Middle–to–Late Holocene explosive eruptions of Lonquimay volcano (Southern Andes of Chile): stratigraphy, tephra dispersal, and pre-eruptive conditions

Jorge E. Romero*[1], Francisco Cáceres[2, 3], Luis Rojas[4], Alicia Guevara[5], Edmundo Polanco[6], Francisca Vergara-Pinto[7], Eleni Michailidou[8], José A. Naranjo[6], Alessandro Fabbrizio[9], Gregor Weber[10], Jorge Bustillos[5], Ángelo Castruccio[12, 13], Matías Poblete[12], and Inés Rodríguez[14].

*Corresponding author: jorge.romero@uoh.cl

[1] Instituto de Ciencias de la Ingeniería, Universidad de O'Higgins, Rancagua, Chile.

[2] Facultad de Ciencias Básicas, Universidad Católica del Maule, Talca, Chile.

[3] Department of Earth and Environmental Sciences, Ludwig-Maximilians-Universität

München, Munich, Germany.

[4] Facultad de Geología, Minas, Petróleos y Ambiental, Carrera de Ingeniería en Geología, Universidad Central del Ecuador, Quito, Ecuador.

[5] Departamento de Metalurgia Extractiva, Escuela Politécnica Nacional, Quito, Ecuador.

[6] Plan Nacional de Geología, Servicio Nacional de Geología y Minería, Santiago, Chile.

[7] Humanitarian and Conflict Response Institute, University of Manchester, Manchester, UK.

[8] Institute of Petrology and Structural Geology, Faculty of Science, Charles University, Albertov 6, 128 43 Prague, Czech Republic.

[9] Dipartimento di Scienze dell'Ambiente e della Terra - DISAT, Università degli Studi di Milano-Bicocca, Piazza dell'Ateneo Nuovo, 1 - 20126, Milano, Italia.

[10] School of Ocean and Earth Sciences, University of Southampton, Southampton, United Kingdom.

[11] Departamento de Geología, Universidad de Chile Santiago, Chile.

[12] Centro de Excelencia en Geotermia de los Andes, Santiago, Chile.

[13] Departamento de Obras Civiles y Geología, Universidad Católica de Temuco, Rudecindo Ortega 2950, Temuco, Chile.

Abstract

The Lonquimay-Tolguaca Volcanic Complex (LTVC), located in Chile's Andean Southern Volcanic Zone (40°S), experienced its last eruption in 1988-90, profoundly affecting neighbouring rural communities. Yet, more than twenty explosive eruptions have been recognised and described at Lonquimay volcano from its Holocene tephra records. Knowing its eruptive past is one of the main concerns of the residents of Malalcahuello, 11 km E-SE from the LTVC. In this contribution, we aim to decipher the behaviour of Lonquimay, focusing on its most recent (i.e., Middle-to-Late Holocene, <5.5 ka) explosive history to address community-based questions with renewed scientific knowledge. We studied proximal-to-medial (i.e., 2-15 km) tephra sequences east-southeast from the LTVC. Seventeen tephra units were described. These are mainly formed by rhythmic alternations of both grey to white pumice beds, and black to brown scoria beds. Pyroclast textures consisting of scoria, dense juvenile fragments and pumices display compositions ranging from basalts to dacites. The study of tephra deposits suggests Strombolian to Sub-Plinian eruptive styles, whereas isopach-based volume estimates on the order of 10^7 m^3 from four individual deposits support a Volcanic Explosivity Index (VEI) of 3. This type of events has a 27-61% probability of occurrence within the next 100 years. The studied tephra deposits were fed by mafic (basaltic and basaltic andesitic, 1050-1100°C) and silicic (andesites and dacites, 890-940°C) magma batches stored between ~2 to ~7.5 kbar. Magma evolution was mostly controlled by fractional crystallisation and occasional mixing events. Assessing tephra fall deposits simultaneously at multiple scales offers clues on the eruptive scenarios, magma processes and sources, as well as potential hazards of their parent volcanic systems. Along with contributing to scientific knowledge, these elements can enhance risk reduction strategies by integrating community questions about active volcanism into hazard research.

Keywords: *Lonquimay volcano; Tephrostratigraphy; Geochemistry; eruption style; Southern Andes.*

1 Introduction

Pyroclastic deposits can be assessed from regional scale (i.e., integration across many outcrops) to microscopic scale (e.g. Houghton and Carey, 2015), involving their correlation from place to place in the field to reconstruct tephrostratigraphy and spatial distribution (Lowe and Alloway, 2014). Further interpretations regarding primary magma fragmentation are based on the grain-size distribution, componentry, morphology, and textural characteristics of juvenile particles (e.g. Walker, 1971; Heiken, 1972; Fisher and Schmincke, 1984; Buttner et al., 1999; Dellino and Liotino, 2002; Zimanowski et al., 2015; Ross et al., 2022). In contrast, an in-depth petrologic study of pyroclasts also provides insights into the pre-eruptive processes that drive volcanic eruptions (e.g. Barclay et al., 1998; Blundy and Cashman, 2008; Putirka, 2008; Smith et al., 2009; Cioni et al., 2008; Re et al. 2021; Wieser et al., 2023; Weller et al., 2024). Therefore, studying tephra sequences at different scales provides information on past eruptive activity, including the frequency of explosive events that is useful to constrain future eruptive scenarios (Cioni et al., 2008; Lowe, 2011). In addition, tephra sequences are a matter of interest and concern for communities that recognise records of explosive eruptions in the landscape (Vergara-Pinto and Marín, 2023; Vergara-Pinto et al., 2024). Questions about what triggered a particular volcanic activity may be common to those residing in and researching a volcanic area, fostering a sense of shared awareness of volcanic hazards. In this way, research can be nurtured by integrating and answering people's crucial volcanological questions. Such attitude reflects the aim of locals to better understand the volcanic phenomena, get involved in risk reduction, and build a collaborative narrative of eruptions with scientists, as in other southern Andes volcanoes (e.g., Vergara-Pinto and Marín, 2023; Alegría and Vergara-Pinto, 2024; Romero et al., 2025).

The Lonquimay-Tolguaca Volcanic Complex (LTVC), located in the Southern Volcanic Zone (SVZ; Fig. 1a) of the Chilean Andes. Lonquimay has experienced at least 22 Holocene explosive eruptions as well as documented historical activity (i.e., 1853–1988; Gilbert et al., 2014). Geological, stratigraphic, and geochemical studies covering the last *ca.* 12 ky eruptive records have provided valuable insights into the Lonquimay's behaviour and eruption frequency (e.g., Polanco, 1998, 2010; Gilbert et al., 2014). However, little is known about its pre-eruptive conditions, genetic eruption styles, dynamics, and distribution of the most recent eruptive activity (i.e., <5 ky BP). This information can be crucial for better constraining the hazard and future eruption scenarios of Lonquimay and for implementing a robust risk assessment policy at the surrounding human settlements potentially at risk (i.e. the Lonquimay town and the Malalcahuello village, Fig. 1b). Nowadays, these territories around LTVC represent diverse growing populations exposed to disaster risk and hope being better prepared for the next eruption (Vergara-Pinto et al., 2024). These communities have developed ways of knowing the volcano through experience, memories, and collectively held imaginaries (Walshe et al., 2023). However, the work of Vergara-Pinto et al. (2024) retrieved volcanological uncertainties of Malalcahuello residents using ethnographic fieldwork and in-depth anonymised interviews (Supplementary Figure 1). Residents highlighted concerns related to different hazards based on volcanic products they observed in their surroundings, such as tephra in road cuts, remnants of pyroclastic deposits in their backyards, and lava flows on the main road (Supplementary Material 1).

In this contribution, we aim to decipher the explosive eruptive history of Lonquimay since the Mid-to-Late Holocene, a task that is closely related to the community-based scientific questions collected in previous research in the study area (Vergara-Pinto et al., 2024). Thus, we use new proximal-to-medial tephrostratigraphy to identify and correlate prominent tephra units, as well as geochemistry and pre-eruptive petrological tools to describe these units in detail. This approach is a natural continuation of the pioneering work of Polanco (1998, 2010) and Gilbert et al. (2014), which were essentially based on medial-to-distal stratigraphy and without detailed analysis of specific units. Our work adds newly recognised events to the whole eruptive record focusing on more localised events in the latest eruptive history of the volcano. Our results can be interpreted in terms of eruptive scenarios, magmatic processes, and volcanic hazards to the communities surrounding Lonquimay.

1.1 Geological and Volcanological Framework

The SVZ (33–46° S) is a volcanic arc that results from the subduction of the Nazca Plate beneath the South American plate and is characterised by more historic volcanic activity than any other volcanically active segment of Chile (Stern et al., 2007), as well as many of the most recent and impactful eruptions of the Andean volcanic arc in the last decades (Romero et al., 2024a). The LTVC represents the northernmost limit of the SVZ's Central segment, defined by Hickey-Vargas et al. (2016) based on geochemical and structural considerations. This segment consists of Middle-to-Late Pleistocene-to-Holocene stratovolcanoes and intra-arc basins tectonically controlled by the Liquiñe-Ofqui Fault System (Fig. 1b; Stern et al., 2007; Cembrano and Lara, 2009). The volcanic products of the SVZ are frequently andesitic, dacitic and rhyolitic, with occasional basalts and basaltic andesites (Stern, 2004).

The LTVC comprises two main volcanic edifices and small eruptive centres aligned in a NE- and ENE-trending fractures. Moreno et al. (2023) consider both edifices as part of a single complex as they erupted synchronously during the late Pleistocene, forming an interbedded volcanostratigraphic sequence in the plateau in between. The oldest main edifice corresponds to the Tolguaca stratovolcano (661 ± 11 – *ca.* 11.7 ka; Moreno et al., 2023), which consists of basaltic to dacitic lava flows and volcaniclastic deposits. On the northwest flank of Tolguaca, Pemehue volcano corresponds to a small polygenetic eruptive centre of basaltic-andesitic to andesitic composition formed at *ca.* 200 ka and which last erupted at *ca.* 11.7 ka BP (Moreno et al., 2023). Lonquimay stratovolcano, which corresponds to the younger edifice of the LTVC, is a small conic edifice compared to the rest of SVZ volcanoes (*ca.* 12 km^3) that reaches 2,865 m asl; in its summit there is a 700–long WSW–ENE elongated crater (Moreno and Gardeweg 1989; Moreno et al., 2023). Lonquimay's evolution has been subdivided into five stages or units (I-V; Moreno et al., 2023): the basal unit I corresponds to glacially eroded basaltic andesite lavas of Late Pleistocene age (*ca.* >130–70 ka), whereas units II-IV are postglacial lavas and tephra of basaltic andesite to silica-rich andesitic composition sourced from the central crater and the northwest flank of the edifice (Moreno and Gardeweg, 1989). Unit V consists of basaltic andesite lava flows sourced from the central vent and flank fissures-oriented WSW–ENE.

In addition to the Lonquimay edifice, Holocene-to-historical activity (1853, 1887–1889, 1936,1940, and 1988–1990; Naranjo et al., 1991) has been sourced from a dozen vents, fissures, tephra cones, and lava domes (Fig. 1b) distributed along a 10 km N55°E structure (Moreno and Gardeweg, 1989). This unit has been named "Conos Monogenéticos Cautín" and includes six historically active eruptive centres made of andesitic-to-dacitic products (Moreno et al., 2023). The youngest centre corresponds to the Navidad cone (Fig. 1b) and its blocky lava flow, formed between 1988–1990 (Moreno and Gardeweg, 1989). The eruption began on December 25, 1988, which formed a cone above the fissure that had been active from 1887 to 1889. The Navidad eruption extended for 13 months producing widespread affectation to livestock (10,000 death of cattle) and human beings (health affectation), plus ash deposition and high concentration of fluorine (Besoaín et al., 1992; Tognetti et al., 2012).

The first tephrostratigraphic studies in the LTVC area were carried out by Polanco (1998) and Polanco et al., (2000) mainly at natural exposed outcrops and roadcuts up to 20 km east of the Lonquimay volcano. These authors identified at least nineteen basaltic to andesitic (49–59 wt% SiO_2) pyroclastic deposits interpreted as tephra fallouts and pyroclastic density currents (PDCs), spanning an age range from 11.23 cal. ka BP up to 1988–1990. The subsequent work by Gilbert et al. (2014) presented a new stratigraphic assessment for these deposits. These were separated into lower, middle and upper Lonquimay tephra sequences (LLS, MLS, and ULS, respectively). The LLS (7.6–11.8 cal. ky BP) mainly comprises mafic phreatomagmatic tephras. The MLS (5.9–7.2 cal. ky BP) contains mafic and intermediate tephras, the latter likely triggered by magma mixing/mingling events as supported by strong oscillatory zoning, mafic enclave incorporation and compositional banding (Polanco, 1998; Polanco, 2010; Poblete et al., 2025). Finally, the ULS (<5.9 cal. ky BP) contains a large proportion of felsic tephras with only scattered mafic clasts and mafic scoria fallouts (Gilbert et al. 2014). Evidence of magma mixing is probably restricted to minor eruptive centres during this stage (Polanco, 2010). To date, the only attempts to quantify the eruption source parameters (e.g., column height and erupted volume) were made on three sub-Plinian Holocene tephra fallouts belonging to the MLS-ULS transition (Polanco, 1998; Poblete et al., 2025).

The products of Lonquimay represent a middle-K, high-Fe, calk-alkaline suite that spans from basalts to dacites (49–65 wt% SiO_2; Moreno and Gardeweg, 1989; Zellmer et al., 2014). These products display FeO_t and Na_2O enrichment and MgO depletion (Moreno et al., 2023). Major and trace elements plus isotopic ratios (Rb/Cs, Cs/La, La/Sm, Nb/Zr, and La/Yb) indicate that its magmas are generated by slab dehydration and partial melting of the mantle and/or slab sediments, with minor to no crustal assimilation, but considerable fractionation and some magma mixing-mingling events (Polanco, 2010).

2 Methodology

2.1 Fieldwork and Sampling

Field campaigns from 2021 to 2025 involved the making of 17 new detailed cross-section descriptions, which were complemented with 26 control sites for tephra observation made between 775 and 1,950 m asl at 3 to 15 km east-southeast from the crater. All of them involved minimal or no reworking. The sites are distributed south of Lonquimay volcano, along new roadcuts of the international 181 highway, and towards the east along the R-785 and R-89 roads. We use pre-existing radiocarbon ages (Polanco et al., 1998; Gilbert et al., 2014) as framework to our study. Twelve of these pre-existing radiocarbon ages were calibrated using the SHCal20 curve (Hogg et al., 2020) in the freeware Calib v.8.2 (Stuvier and Reimer, 1993; Supplementary Material 2). In addition, we carried out an additional ^{14}C dating on charcoal fragments found at LQ1 from a PDC, giving an age (58% probability) of 231-138 cal. BP. The analysis was made at Beta Analytic, Florida. Based on the initial assessment for the Lonquimay tephra fall sequences (LLS, MLS and ULS) made by Gilbert et al. (2014), our work focuses on a detailed characterisation of the ULS. Previously, these authors identified and named seven tephra fall deposits (Units Q to W), for which they provide geochemistry and some petrological characteristics. We now extend these records for tephra deposit correlation in newly recognised sites based on their stratigraphic position, lithological components, pyroclastic texture, tephra internal architecture (e.g., particle size, grading, bedding, etc.), unconformities and soil horizons (Table 1). Former and newly described units were named based on type localities (when possible) or diagnostic characteristics translated to the Mapudungun language (honouring the native people of the area, i.e., Mapuche Pewenche; Table 1).

Bulk deposit volume estimates were computed from isopachs drawn based on our field measurements of tephra thicknesses for three different deposits. We used the AshCalc tool (Daggitt et al., 2014) to integrate tephra volumes based on the area and thickness of tephra deposits, applying both the exponential thinning and Weibull models (Pyle 1989; Fierstein and Nathenson, 1992; Bonadonna and Costa, 2012) as in Romero et al. (2021). Individual datasets have a small number of homogeneously distributed field tephra thickness measurements (i.e., 10-20); these should consider up to 63% error in volume estimates, with the average error from 20 to 33% (Romero et al., 2024b). In this regard, we consider an average uncertainty of 33% for the resulting volume estimates.

We obtained fifteen bulk tephra samples that thirteen recognised pyroclastic units. The samples were dried at 60°C for 72h. These samples' largest representative juvenile clasts (i.e., of the overall juvenile population) were selected for further textural and petrographic investigation.

2.2 Geochemistry and Mineralogy

We conducted X-ray fluorescence geochemical analyses on sixteen samples at the Departamento de Metalurgia Extractiva de la Escuela Politécnica Nacional in Ecuador

(DEMEX-EPN). These corresponded to pumice and scoria samples from representative tephra units presented in this study (Table 2). Samples were crushed in an agate mortar (1 g) and mixed with lithium metaborate. A melted bead was produced using a platinum melting pot in the Katanax fusion fluxer. The glass beads were analysed using a Bruker S8 Tiger XRF instrument and the Spectra Plus software, identifying major oxides (SiO_2, Al_2O_3, TiO_2, MgO, CaO, Na_2O, K_2O, P_2O_5 and total iron as Fe_2O_3) with the loss on ignition (LOI) values never higher than 3.2% (Table 2). Both instruments have detection limits of 0.1 wt.% for major oxides. Data was normalised to a water- and LOI-free basis and complemented with data found in the literature.

Electron probe microanalyses were carried out simultaneously at the Department of Earth and Environmental Sciences from the Ludwig Maximilians Universität München (Germany), using a Cameca SX100, and the JEOL JXA-8530F at the Institute of Petrology and Structural Geology, Charles University (Czech Republic). We used the same analytical conditions in both facilities: 15 keV of acceleration voltage, 40 and 5 nA of beam current, and 1-10 µm defocused beam, for mineral phases and glass, respectively. In all the analyses, Na was measured first to avoid its loose, in TAP position. Otherwise, Na loss during analyses would impact geothermobarometric estimates, specifically those based on pyroxene (e.g., Wieser et al., 2023). There is evidence that in pyroxene with relatively low Na_2O contents (i.e., augite), there is no need to restrict count times or beam currents, as Na migration seems negligible (Wieser et al., 2023). Counting times were 10s peak measurement and 2 times 5s background measurement for all elements, except Mn, for which it was 20s peak measurement and 2 times 10s background measurement. We used the following standards: albite (Na), orthoclase (K), synthetic Al_2O_3 and corundum (Al), Springwater olivine (Si, Fe, Mg), calcite and wollastonite (Ca), rutile (Ti), rhodonite and bustamite (Mn), Cr_2O_3 (Cr), apatite (P), vanadinite (V, Cl), and anhydrite (S). We used quartz, magnetite, periclase, topaz, and halite for Si, Fe, Mg, F, and Cl, at Charles University. The ZAF correction was used to reduce the data. In total, we carried out 818 spot measurements. These correspond to 443 plagioclase, 74 apatite, 28 pyroxene, 139 olivine, 14 Fe-Ti oxides, and 120 groundmass glass (Supplementary Material 3). In this instrument, uncertainty is between 1 and 5% for major elements and up to 10% for trace elements (< 0.2 wt%).

2.2 Geothermobarometry

To obtain a variety of estimates to constrain pre-eruptive magma storage pressures and temperatures, we tested a range of thermometers and barometers on our mineral-melt compositions (Supplementary Material 4). We used the machine learning thermobarometer for clinopyroxene-bearing magmas of Ágreda López et al. (2024) to obtain pressure and temperature estimates based on the major element chemistry of clinopyroxene-only and clinopyroxne-liquid pairs. We also used the machine learning thermobarometer of Weber and Blundy (2024), applied to matrix glass and whole-rock compositions as a proxy of melt composition and the associated mineral assemblages of these rocks. Both models are based on an extremely randomized trees - random forest approach, using an ensemble vote of decision trees. In this setup, decision trees make predictions (i.e. pressure or temperature) by repeatedly random splitting data into branches based on randomly selected feature values (i.e. composition), with each branch leading to an outcome at the leaves. In a random forest, the outcomes of many decision trees (typically >500) are averaged to predict the variable of interest.

The model of Ágreda López et al. (2024) has been calibrated on a curated set of experimental clinopyroxene-liquid pairs, spanning a broad compositional spectrum from basalt to rhyolite including those from arc environments, a pressure range of 1-atm to 30 kbar, and temperatures between 650-1800°C. To test equilibrium, we filtered the cpx-liquid pairs with K_D(Fe-Mg)$^{cpx-liq}$ = 0.28 ± 0.08 (Putirka, 2008). Only cpx-liq pairs with measured K_D values within ± 0.1 of the predicted values calculated were accepted. Testing of the model is cited with a Root-Mean-Square-Error (RMSE) of 57°C and 2.5 kbar for the cpx calibration, and 36°C and 2.1 kbar for the cpx-liq calibration. All clinopyroxene calculations were carried out using their web application: https://ml-cpx-thermobarometry.streamlit.app/.

The Weber and Blundy (2024) geothermometer and geobarometer is calibrated on experimental data ranging from basalt to rhyolite, pressures from 0.2 to 15 kbar, and temperatures of 675 °C to 1400 °C. Weber and Blundy (2024) tested the model performance on experiments not used in the calibration, resulting in RMSE from 1.7 to 1.9 kbar and RMSE on temperature estimates of 36-42°C. They also showed that these errors can be further reduced to 1.1-1.3 kbar and 21°C by filtering out the results that show high standard deviation in the ensemble vote of the random forest. The model is applied on pairs glass compositions and associated stable (equilibrium) mineral assemblage to estimate last equilibration pressures and temperatures. An alternative approach is to use the model on pairs on bulk rock compositions and mineral assemblages to estimate the melt extraction source depth in crystal mushes (see discussion in Weber and Blundy (2024) for further details). All these calculations were performed online using the web application MagmaTAB (https://igdrasil.shinyapps.io/MagmaTaBv4/). Temperature estimates were not filtered as the impact on the results was minor. Given the larger pressure uncertainties, the results were filtered as discussed above by removing estimates greater than the 70th percentile of the random forest ensemble vote. Pressure was converted into apparent depth assuming a constant crustal density of 2700 kg m^{-3} (Tassara and Echaurren, 2012).

We also tested a wide range of commonly applied, conventional methods (i.e. non-machine learning; Nimis, 1995, Nimis and Ulmer, 1998, Putirka, 2008; Neave and Putirka, 2017; Wang et al., 2021). For the specific case of olivine-liquid models, we filtered our data to reflect equilibrium condition with K_D(Fe-Mg)$^{ol-liq}$ = 0.30 ± 0.03 in accordance with Roeder and Emslie (1970) for basaltic systems, at P < 20–30 kbar. However, on our dataset these models produced results that were conflicting with each other (Supplementary Materials 4). We therefore do not further consider these estimates. In addition, the glass-based model of Fabbrizio and Špillar (2020) was applied for those olivine-bearing glassy samples.

We estimate H_2O contents by using the web application of the plagioclase-saturated melt hygrothermobarometer of Cutler et al. (2024) (https://kyra-cutler.shinyapps.io/PlagSat/). We used 111 groundmass glass compositions that were tested for plagioclase saturation after comparing major oxides with calibration experiments. After that, we computed H_2O/T-independent anorthite contents, temperature, H_2O, and pressure. All the results were filtered to 0.75 SD, and the anorthite contents were checked for match with the EPMA results. These results have RMSEs of 25°C, 0.70 wt.% and 0.76 kbar.

3 Results

3.1 Stratigraphy

Tephra preservation at LVC mainly occurs eastwards of Lonquimay volcano, along the Cordillera de las Raíces range, towards Lonquimay. Proximal exposures are found on the Lonquimay flanks (<3 km from the central crater); these outcrops are only covered by scarce herbaceous shrubs and juvenile *Araucaria araucana* trees. Tephra sequences may reach >10 m in thickness and are exposed by streambank erosion in ravines and gullies (Fig. 2a) but also found at inclined slopes, especially towards the southeast of the main edifice. They consist of superposed tephra beds, 25–130 cm thick each, containing clast supported, well sorted coarse lapilli to bomb-sized juvenile clasts composed of pumice or scoria that represent tephra fall deposits. Proximal outcrops also contain a limited number matrix-supported ash beds containing lapilli clasts, occasionally developing sedimentary structures (e.g., cross bedding, dune bedforms, etc.) that we interpret as deposited by pyroclastic density currents (PDCs, Fig. 2b). In proximal areas there are no paleosols intercalated between the individual pyroclastic units (Fig. 2c). In contrast, medial exposures (3–15 km from the main crater) are primarily located along the Cordillera de las Raíces mountain range and correspond to gullies formed by creeks (Fig. 2d) and roadcuts along the R-89 mountain road. In these areas, the stratigraphy is characterised by subhorizontal tephra fall beds composed of scoria and pumice up to 80 cm thick that are occasionally intercalated with reworked tephra deposits, alluvial beds, and paleosols (andisols). An erosive angular unconformity marks a sharp transition that separates the MLS and ULS (*ca.* 5.9 ka BP; Fig. 2e), constrained to 7.6–5.9 ky BP (Gilbert et al., 2014). Another erosive unconformity separates the MLS from the LLS (7.6–11.8 ky BP; Gilbert et al., 2014). For distal exposures (>15 km), outcrops encompass sequences that are mostly formed by thin (<15 cm) weathered tephra deposits interrupted by prominent andisols. These areas are more vegetated, with native old-growth stands and trees up to 40–50 m tall (Tognetti et al., 2012) that may reach up to 1700 m asl.

We present the new composite tephrostratigraphy of the ULS (Fig. 3), which accounts for 17 tephra deposits. Other deposits couldn't be correlated because of their poor preservation. All these units distribute in the E flank of the volcano and comprise the thickest field exposures, mostly based on the most complete pyroclastic sequences found at sites LQ18, LQ33, LQ36, and LQ38, which are located at distances <5.6 km southeast of the volcano (Fig. 4). Also, a comprehensive Holocene tephra section is found ~10.7 km northeast (LQ25). All the stratigraphic sites south of Lonquimay volcano exhibit scattered ULS tephras (Fig. 4).

In all these proximal-to-medial stratigraphic sections, the oldest recognised tephra deposit corresponds to La Negra (LN, 5,504-5,446 cal. yr BP). Two other distinctive tephra fall deposits lie stratigraphically on top of the LN: Pewenkura (PK; 4,362-3,778 cal. yr BP) and Manto Amarillo (MA, 3,778-3,262 cal. yr BP) (Polanco, 1998). These three deposits are studied in detail in a companion paper by Poblete et al. (2025), which focuses on their eruptive parameters and pre-eruptive conditions. Therefore, we mainly focus on tephras overlying MA.

The sequence overlying MA is mainly characterised by rhythmic alternations of grey to white pumice beds and black to brown scoria beds of tephra fall origin (Table 1). From at least four recognised pumice units, the most remarkable correspond to Liqkura (LI; 4,415-2,648 cal. yr BP, known as LQU by Polanco, 1998), Alikura (AK; 1,294-391 cal. yr BP; Gilbert et al., 2014), and Külleg (KU) (Fig. 3).

Scoria beds that overlie MA (i.e., <3,778 cal. yr BP; Polanco, 1998) correspond, from base to top, to Dumiñmapu (DM), Kurumawün (KM), Pumakuñ (PU), Wikür (WK), Corralco (CO), Cautín (CU; 194-162 cal. yr BP; Polanco, 1998), and Navidad (NV) (Figs. 3 and 4). In addition to these, other tephras cannot be correlated because of their poor preservation or scattered presence in the field sections.

In addition to tephra fall, two deposits interpreted as pyroclastic density currents are also recognised: Kurütrufken (KT) and Malalcahuello (ML). Both are composed by scoria clasts supported in ash-sized juvenile matrix and occasionally contain cross-bedded structures (Table 1). From charcoal within the ML deposit, we obtained a calibrated age of 231-138 yr BP, this work). Therefore, it likely represents the youngest PDC deposit in the sequence.

Also, three other massive, well sorted and clast supported deposits are mostly composed of subrounded to subangular dense juvenile clasts with varying content of hydrothermally altered clasts. They correspond, in stratigraphic order (older to younger) to Kadü and Kürutrongen and have only been described at sections LQ18 and LQ33 (Fig. 4).

3.2 Distribution and volume

All the thicknesses and isopachs presented in this section, except for the NV deposit (Naranjo et al., 1991), are original from this work. The KM deposit is distributed ~N126°E, and its preserved thicknesses range from 10 to 110 cm. The outer isopach (10 cm) covers an area of ~136 km^2. The computed volume ranges between 55 ± 18 x 10^6 m^3 and 74 ± 24 x 10^6 m^3. The AK deposit has a complex dispersal with two lobes (~N110°E and ~N160°E; Fig. 5), with its most distal isopach constrained to 5 cm. The 10 cm isopach covers ~226 km^2 and the total tephra fall deposit volume ranges from 46 ± 14 to 51 ± 15 x 10^6 m^3. Finally, the CU deposit is the smallest, and the measured thickness (3 to 245 cm) rapidly decreases towards the southeast (~N126°E; Fig. 5), with its 10 cm isopach covering ~17 km^2. Its volume results in 13 ± 4 x 10^6 m^3. For comparison, the NV deposit accounts for 59 ± 18 x 10^6 m^3 and 98 ± 29 x 10^6 m^3 according to the isopachs drawn by Naranjo et al., (1991), from which the 10 cm isopach covered ~74 km^2 (Fig. 5), being the most volumetric of the studied tephra fall deposits. This is probably due to the detailed control on the distal portion of the deposit, from which the most distal isopach (1 cm thick) covered nearly 1160 km^2. In addition to these tephra fall deposits, we determined the approximate distribution of the ML and KT PDC deposits using field control points and topographic maps. ML has an average thickness of 0.32 m and covers ~16.9 km^2, which yields a rough volume estimate of ~5.42 x 10^6 m^3. KT is much smaller, with an average thickness of 0.26 m and covers 3.4 km^2, thus resulting in a rough volume estimate of ~0.9 x 10^6 m^3.

3.3 Pyroclast texture

The juvenile products correspond to (1) fusiform scoria and blocky scoria, (2) dense juvenile fragments, and (3) pumices. These types are related to different compositional groups, namely basaltic to dacitic; blocky and fusiform scoria could coexist in both basaltic and basaltic andesitic compositions. These categories are better described in the section of "composition and mineralogy": (1) Blocky and fusiform scoria shows ragged exteriors, sometimes fluidal shape, and jagged perimeter (e.g., units LN, DU, PU, WK and CO; Fig. 3). These pyroclasts contain tabular plagioclase feldspar and occasionally pyroxene phenocrysts within the glassy groundmass (vitrophyric texture). Sometimes, due to syn-eruptive oxidisation or post-depositional weathering, these pyroclasts display a reddish colour (e.g., KM and CA; Fig. 3). Fusiform pyroclasts with external ropy texture are also recognised as in the NV proximal deposit (Fig. 3). (2) Grey, dense (low vesicularity, <25 vol.%), aphanitic subangular lapilli shows external flat surfaces and straight borders (e.g., KA; Fig. 3). (3) White, light-brown, yellow or pinkish moderately vesicular (i.e., 25-50 vol.%) subrounded to subangular pumice is present in units PK, LI, KL, and AK (Fig. 3). The vesicles are generally elongated to filamentous forming narrow inter vesicular walls. This pumice develops vitrophyric to aphanitic texture.

Other deposits, such as KT, mostly contain finer particles (Fig. 2, 3; fine-to-coarse ash size) that correspond to sub-millimetric juvenile grains including glass shards and free crystals of plagioclase, pyroxene, and olivine.

At a microscale, basaltic scoria displays vesicles ranging from ~30 µm up to 2 mm in length. They could contain up to 15 % vol. phenocrysts (plagioclase + olivine ± clinopyroxene ± oxides). Vesicles (~55%) are irregular to convolute in shape and they readjust around phenocrysts (mostly tabular plagioclase and olivine) (Fig. 6). Subhedral to euhedral plagioclase phenocrysts can exhibit concentric oscillatory zoning and sieve (spongy cellular) texture. In the groundmass, vesicles are scarce, and their shapes are subspherical. The groundmass mainly contains tabular, prismatic, and acicular euhedral to subhedral plagioclase phenocrysts plus granular olivine and pyroxene dendrites in addition to interstitial glass (Fig. 6). The basaltic andesite pyroclasts can either display less vesicularity (~45 vol.%) with narrower size variability (~100 µm to 1 mm), less irregular shapes and modest vesicle interconnections, or be highly vesicular (~70 vol.%) with subrounded to ellipsoidal shape bubbles (~50 µm to 800 µm) and some preferential flow orientation (Fig. 6). The crystal content is low (<5%) and consists of plagioclase + olivine ± pyroxene ± oxides. Between these two types of pyroclasts, differences also include the degree of crystallisation vs. glass at the groundmass scale, and the size of microlites: extremely vesicular clasts contain acicular pyroxene and euhedral plagioclase microlites within a glassy groundmass, whereas the less vesicular have groundmasses with prismatic and tabular euhedral plagioclase, pyroxene with incipient dendritic branches, granular olivine and Fe-Ti oxides (Fig. 6). In some cases, skeletal olivine is also observed. Andesitic and dacitic pyroclasts are very similar and contain a large proportion of vesicles (>70 vol.%), showing spherical, subspherical, and stretched elongated vesicles (~10 µm to ~700 µm), mainly oriented with the flow direction, with abundant inter-vesicular groundmass glass and scarce acicular plagioclase microlites (Fig. 6). Phenocrysts are rare and can represent only 1-3%; however, they mainly consist of subhedral plagioclase, euhedral and subhedral Fe-Ti oxides and pyroxene.

In addition to juvenile material, lithics in pyroclastic deposits correspond to aphanitic to porphyritic, plagioclase bearing, subangular to subrounded, low-vesicularity rock fragments with variable degrees of weathering and oxidisation.

3.4 Composition and Mineralogy

The suite of normalised and LOI-free whole rock compositions (Table 1) spans from basalts to dacites (51.3–68.0 wt% SiO_2; Fig. 7a). All the rocks are calc-alkaline, and they have medium-K content with modest variations of K_2O (0.5–1.7 wt%; Fig. 7b). From the total alkali vs silica diagram, we identify at least four different compositional clusters of tephra compositions: the basaltic and basaltic-andesite ones, which represent narrow variations in the SiO_2 contents (51.3–52.2 wt% and 54.4–55.6 wt%), an andesitic cluster (58.8–62.5 wt%), and a dacitic cluster (62.5–68.0 wt%). Na_2O behaves as an incompatible element and slightly increases with differentiation from c. 3.7 to 5.7 wt% in basaltic andesites to dacites, as well as K_2O that increases from 0.5 to 1.7 wt% (Supplementary Fig. 2). All other elements behave compatible and decrease linearly with differentiation (Supplementary Fig. 2).

Groundmass glass compositions of the same rock suites are enriched in SiO_2 (3-8 wt% excess) and depleted in alkali (up to ~2 wt%; Fig. 7a), with medium-K (calc-alkaline) affinity (Fig. 7b) compared to their whole rocks. In this respect, Na_2O displays lower values in the glass groundmass compared to whole rock. Rather than explaining this depletion by Na loss during microprobe measurements, which was carefully controlled, we attribute this behaviour to the degree of fractionation as this element is used in the crystallisation of albite (e.g., Arzilli et al., 2019). The least evolved glass is basaltic andesite (55-58 wt% SiO_2), whereas the most evolved one is dacitic-rhyolitic (68.5-72 wt% SiO_2). A previous investigation by Gilbert et al. (2014) found that the K_2O/TiO_2 vs SiO_2 diagram was useful to distinguish between different compositional groups of Lonquimay tephras, from which we observe that the clustering proposed above fits well also for glass compositions. We also notice that the andesitic and dacitic products in the Polanco (1998) dataset display great dispersion (Fig. 7c). Such dispersion in a few samples is mainly produced by the K_2O excess (~0.5 wt.%) from the main linear trend in a SiO_2 vs. K_2O plot. By plotting FeO_T/MgO vs. CaO/Al_2O_3, it could be possible to distinguish the trends of mineral phase fractionation and possible mixing, as this plot is frequently used as a differentiation index in systems that crystallise clinopyroxene, olivine, and plagioclase (e.g., Di Carlo et al., 2006; La Felice and

Landi, 2011). While most of the basaltic glass compositions may indicate a clinopyroxene crystallisation trend, and most of the whole-rock and intermediate-silica glass follow a trend of plagioclase + olivine + clinopyroxene differentiation (Fig. 7d), some of the glass compositions from the basaltic and andesitic rocks approach the mixing trend (Fig. 7d). Such glass composition scattering, especially for the glass of andesitic rocks is also visible in the other plots (Fig. 7a-7c).

If analysed in a stratigraphic disposition, we observe a "cyclic" whole-rock variation from most silicic end members (andesites and dacites) towards basaltic andesites and basalts (e.g. from tephras Liqkura to Kurumawün) or the way back from mafic to more silicic compositions (e.g. La Negra-Pewenkura, Dumiñmapu-Liqkura, Kurumawün-Alikura or Corralco-Cautín pairs) that generally involve a pair of tephras in sharp stratigraphic contact (Fig. 7e). In the case of the Cautín tephra, its composition also varies from bottom to top towards a more silicic composition. Such syn-eruptive changes should be studied in greater detail because they have not been investigated in this research.

Plagioclase phenocrysts are euhedral to subhedral with prismatic or tabular shapes and sizes between 200 to 500 µm, while plagioclase microlites are generally prismatic, euhedral and have sizes < 50 µm. The latter are distributed in the groundmass, occasionally showing orientation. The mineral chemistry of plagioclase feldspar comprises a wide range of compositions ($An_{17–71}$). Significant variation from bytownite to anorthoclase (Fig. 8a) is observed in plagioclases from andesites. However, most data are in the range of labradorite-andesine, including plagioclases in basalts and basaltic andesites ($An_{45–71}$ and $An_{40–56}$, respectively). A similar diversity is observed from existing data for the Lonquimay volcano and the 1988–90 eruption of the Navidad cone (Fig. 8a; Polanco, 2010; Macomber, 2015). Disequilibrium textures (embayment and sieve textures) can occur in larger phenocrysts embedded in mafic or intermediate rocks and within mafic enclaves that exist in these rocks, thus in the form of antecrysts. In pumice and very vesicular scoria, plagioclase crystals are fractured but do not show disequilibrium textures, and we consider them as autocrysts.

Olivine occurs as granular phenocryst in the basaltic and andesitic basaltic samples, with sizes of 100-200 µm and subhedral to anhedral shape. In the ML sample, olivine phenocrysts have a marked fayalitic composition (Fo_{28-31}; Fig. 8b) form crystal clots with clinopyroxene and Fe-Ti oxides. In some cases, Fe-Ti oxides, apatite and clinopyroxene are present as small (<100 µm) poikilitic inclusions within these olivine crystals. The olivine phenocrysts from three different NV samples are all low forsterite (Fo_{46-64}; Fig. 8b) irrespectively if they are phenocrysts or microlites, and the larger phenocrysts (antecrysts) show embayment, dissolution, and skeletal textures. In contrast, all the olivine grains in the KM sample are forsterite-rich (Fo_{58-71}; Fig. 8b) and do not exhibit disequilibrium textures, but reverse zoning with 1-2 Fo % can be measured in transects towards the rims (Supplementary Material 3) and are considered autocrysts.

All the samples contain pyroxene, but it represents nearly 1% of the sample components. They consist in subhedral to euhedral phenocrysts with tabular shape, 150-300 µm size, and in basaltic or basaltic andesites they also form microlites. Clinopyroxene crystals from basaltic andesites display in a narrow range (En_{55-60}), with a slight enrichment in the Wo component (Fig. 8c), falling in the same compositional fields reported by Polanco (2010) and by Macomber (2015). None of them present disequilibrium textures.

Fe- Ti oxides are present in all samples and are anhedral to subhedral in shape. Their sizes are generally smaller than 200 µm in the basic and intermediate samples, while in the more siliceous samples the sizes are larger, between 200-500 µm. Fe-Ti oxides measured in basaltic andesites and dacites contain ~74 wt.% FeO_T and ~22 wt.% TiO_2.

3.5 Pre-eruptive conditions

The results of the multiple thermobarometric methods are generally in good agreement with each other (Fig. 9). In total, 64 olivine phenocrysts where in equilibrium with their melts (K_D 0.24-0.30). In basalts, forsteritic (Fo_{58-71}) olivine is equilibrated with a basaltic-andesitic melt (~52 wt. SiO_2; whole-rock composition) and returns a median temperature of 1075 ±3℃ (1SD). These results are in good agreement with the glass-assemblage model (1076±12℃) but differ from whole-rock assemblage calculations that inform higher temperatures (1113±4℃). Like the basalts, basaltic andesite temperatures are convergent between the different methods: ol-liquid (1088±34 °C), cpx-only (1073±12 °C), cpx-liquid (1054±20 °C), and bulk rock-assemblage (1066±14 °C) methods. In this case, the glass-assemblage method recovers lower temperatures (953±22 °C), which is likely related to the presence of microlites in the glass that yield to a residual glass composition. In consequence, these values were discarded from Fig. 9. Interestingly, Fayalite-rich olivine (Fo_{28-31}) present in the KM basaltic andesites are in equilibrium with more evolved, andesitic and dacitic groundmass glass (~ 68% SiO_2), but the autocrysts of Forsterite-rich olivine present in the NV samples (Fo_{46-64}) fit better with more mafic groundmass glass compositions (~62-63 wt. SiO_2). In general, andesitic and dacitic samples (alongside a few andesitic compositions) return much lower temperatures compared to basalts and basaltic andesites, ranging from 870 to 1030 °C, as using the MagMaTaB model (Weber and Blundy, 2024). These results both consider groundmass glass and whole-rock compositions alongside mineral assemblages of these rocks.

The same mineral-melt, mineral only, and melt-assemblages were used for the barometry (Fig. 9). Cpx-only and cpx-liquid for basaltic andesites return a whole range of values of pressures from ~0.4 to ~9.5 kbar, corresponding to ~1.5 to ~35 km depth. Contrastingly, the estimates obtained using the glass- and whole-rock assemblages range from ~2.1 to ~5.1 kbar, which correspond to ~7 to ~19 km depth. Only basaltic and basaltic andesites suggest higher pressures in the whole-rock assemblage models (4.3 to 9.5 kbar or ~16 to ~35 km depth) that could correspond to the deeper primitive magma intrusions in the system.

Using the Cutler et al. (2024) hygrothermobarometer, we obtained 28 temperature, H_2O, and pressure estimates from the initial 111 compositions. Only one H_2O estimate was obtained for each ML and KM units (6.7±1.5 and 0.0±0.4 wt.%, respectively), while for the CU dacite it yielded 6.4±1.6 wt.%. For all the NV estimates, the H_2O content is 0.0-0.8±1.7. All the compositions inform temperatures of 843-1109 °C pressures of 2.1±1.7 kbar.

4 Discussions

4.1 Eruptive style

Our eruptive style interpretation is based on the tephrostratigraphy plus the external and internal juvenile pyroclast textures.

External fluidal textures or ragged scoria surfaces in these deposits, in addition to their moderate vesicle content (~45–55%) and vesicle shapes observed in basaltic and some basaltic andesite pyroclasts (i.e., KM and NV), are usually reported for explosive lava fountain eruptions (e.g., Polacci et al., 2006; Houghton and Gonnermann, 2008). For paroxysmal eruptions on Etna, Polacci et al. (2006) described these vesicles as large (hundreds of microns to >1mm) of convoluted and irregular shapes that denote extensive coalescence and readjustment around plagioclase, pyroxene, and olivine phenocrysts. These textures are also observed in the 2015 lava fountain of Villarrica volcano (Romero et al., 2023) and differ from those formed by typical Strombolian eruptions, which generally contain spherical vesicles with low coalescence (Moitra et al., 2013; Kósik et al., 2016). These textures are also like those of basaltic Plinian eruptions (e.g., Moitra et al., 2013). This interpretation is well in agreement with the direct descriptions of the 1988–90 Navidad cone's eruption (Moreno et al., 1989; Naranjo et al., 1991, 1992) that led to the formation of the NV deposits, which also exhibited a hybrid behaviour featured by simultaneous lava and tephra emission (Bonadonna et al., 2022). On the other hand, pumices exhibited a high proportion of sub-spherical to elongated stretched vesicles (>70%) and almost crystal-free groundmass glass. These textural features are comparable with those from products of highly explosive (i.e., sub-Plinian) intermediate-to-silicic eruptions (e.g. Alfano et al., 2012; Pistolesi et al., 2015; Martel et al., 2021). In fact, pumices with similar texture, vesicle content, and shape to our andesites and dacites of Fig. 7, have been interpreted as produced by rapid heterogeneous vesiculation kinetics inside changing conduits and intense strain rate during the 3,300 cal BP Upper Inglewood eruptive episode of Taranaki volcano (Torres-Orozco et al., 2023). The pumice deposits of Lonquimay volcano were formed by a single-graded or multiple-bed deposit, thus indicating both sustained and intermittent or non-sustained eruptions, according to Houghton and Carey (2015). The average estimated bulk volumes for all the studied tephra fall deposits (KM, AK, CU and NV) is $\sim 10^7$ m^3; thus, Volcanic Explosivity Index 3 eruptions (VEI, Newhall and Self, 1982) in the range of Strombolian to small sub-Plinian events. Therefore, we discard these eruptions were Plinian; they likely represent violent Strombolian or lava fountaining events. In addition, the multi-bed architecture of many deposits (e.g., LN, PW, DU, KM, PU, and CU) informs intermittent and non-sustained discrete eruptions consisting of many short-lived pulses or the occurrence of small column collapses during the eruptions (Houghton and Carey, 2015). The studied tephras were transported by prevailing westerly winds and deposited eastward of the volcanoes in proximal mountainous localities, as it has been typical during the Holocene ASVZ (e.g., Fontijn et al., 2016). However, since we only examined sections east of the LTVC, it is possible that tephras with different dispersion patterns are underrepresented in our research. Furthermore, it is possible that smaller eruptions have not been preserved in our stratigraphic record, which would affect its integrity.

On the other hand, the internal textures of pyroclasts belonging to basaltic andesites and andesites are an intermediate member between basaltic and dacitic end members, and their variable vesicularity (up to ~70%) and even the presence of "dense" juvenile clasts can be interpreted because of syn-eruptive magmatic degassing resulting in microlite growth prior to fragmentation (Gardner et al., 1998), as also observed in their groundmasses (Fig. 6). These pyroclasts can also result from dome growth and magmatic column stratification during Vulcanian events (e.g., Romero et al., 2017; Cole et al., 2024). They are present either as deposits containing predominantly dense juvenile material (such as KA, KD and PU) or a lithic-dominated basal layer at the base of AK, with both unaltered and hydrothermally altered dense clasts that may represent parts of a plug or the conduit (Table 1). It is worth noticing that Gilbert et al. (2014) did not recognise the grey-dense pyroclasts within the ULS tephras, despite they are frequent at the middle of the ULS.

4.2 Insights into magmatic processes

Whole-rock compositions and groundmass glass geochemistry of selected pyroclasts show a semi-continuous compositional range from basalts to andesites, with an apparent clustering of specific compositions for basalts, basaltic andesites, andesites and dacites (Fig. 7a-f). They are also characterised by compositionally restricted suites of K_2O/TiO_2 vs. SiO_2 (Fig. 7e, f). Although this feature could be a result of data representativeness, previous analyses by Polanco (2008) and Gilbert et al. (2014) on ULS samples plotted for comparison also show similar compositional clustering (Fig. 7a-b). The FeO_T/MgO vs. Ca_2O_3/Al_2O_3 trends may be interpreted as individual magma differentiation/evolution stories that include fractional crystallisation and sporadic mixing events (e.g., Di Carlo et al., 2006; La Felice and Landi, 2011). In this respect, some basaltic and basaltic-andesitic glasses show dispersion indicative of magma mixing, while most of the basaltic-to-dacitic samples follow the fractionation trend. Crystal fractionation is supported by whole-rock major-element linear trends in Harker diagrams, but also by mineralogical assemblages consisting of a plg ± ol ± cpx ± opx ± ox. Most of the existing crystals are therefore autocrysts, lacking disequilibrium textures. In addition, they display a continuous compositional evolution, from anorthite-albite crystallisation from mafic to felsic rocks and wide range of olivine compositions, from fayalite to forsterite-rich. However, disequilibrium textures are particularly abundant in basaltic andesites, mainly producing olivine resorption textures (including rounded crystals and skeletal textures; Supplementary Fig. 3a, b), plus plagioclase with spongy-cellular sieve texture (Supplementary Fig. 3c, d). This is the case of the NV tephra, containing skeletal olivine crystals (Fo_{46-64}) that equilibrate with intermediate (~62-63 wt. SiO_2) at low-water contents (<0.8 wt.%). These features are typical of magma mixing events (e.g., Thornber and Huebner, 1985; Streck, 2008; Salas et al., 2021). Another interesting evidence is the wide range of pressures obtained for these rocks: ~0.4 to ~9.5 kbar, compared to the other rocks that display a more restricted range of pressures (~2.1 to ~5.1 kbar). The case of ML containing fayalite and low anorthite plagioclase (An_{21-44}) requires further explanation.

Fayalite crystals are only equilibrated with high-silica liquid compositions associated to high-water content (6.7 wt.%). Similar fayalite-bearing assemblage has been reported in the lava domes and pyroclasts sourced from the peripheral Conos Monogenéticos Cautín, which have dacitic and trachytic composition. Poblete et al. (2025) explains fayalite in these rocks because of excess FeO_t, which under reducing conditions promotes Fe^{2+} incorporation in mineral phases at very low pressure and high-water content. However, the whole-rock basaltic-andesite composition of ML scoria could suggest that these shallow evolved melts were removed by the interaction with more mafic magmas. Therefore, we propose that fractional crystallisation controls the differentiation from basalts to dacites at Lonquimay volcano, however this trend is interrupted by mixing events driven by deeper mafic injections into cooler, more crystallised, and shallower felsic magma batches.

The latest evidence points to the importance of crystal remobilisation and incremental magma recharge in assembling these magmas, aligning with the interpretations of Gilbert et al. (2014). This mechanism is further supported by the oscillatory eruptive behaviour observed (Fig. 7g), a hallmark of recharge-driven systems as seen in other stratovolcanoes such as Merapi (Gertisser and Keller, 2003). In fact, we observe that the Middle-to-late Holocene Lonquimay tephras show apparent inter-eruptive cyclic variations between mafic and silicic products and occasionally within a single unit (Fig. 7g, i.e. Cautín tephra). These processes can be controlled by the progressive eruption of stratified portions of fractionated magma reservoirs that erupt either mafic or silica-rich products, being occasionally interrupted by mixing events that result in the eruption of intermediate magmas, such as the NV eruption. The wide compositional range and temperature bimodality observed are consistent with thermal models of high-flux magmatic systems still in an early stage of development (Melekhova et al., 2013; Weber et al., 2020).

Focussing on our new thermobarometric estimates, these are generally consistent with previous results (e.g., Polanco, 2010; Gilbert et al., 2014; Poblete et al., 2025) and indicate that the Lonquimay explosive eruptions are primarily fed from a region between 7 and 19 km depth. These estimates suggest a potentially vertically extensive magmatic system (e.g. Cashman et al., 2017). The results are also in good agreement with storage zones between 5.6 and 12 km proposed by Poblete et al. (2025) for tephras LN and PK. However, given typical barometric uncertainties (~2 kbar), a narrower magma accumulation zone cannot be ruled out. Interestingly, Gilbert et al. (2014) applied hornblende and cpx-liq thermobarometry to LLS and MLS tephra. However, as they noticed, hornblende is no longer present in ULS tephras, which requires further tectono-magmatic investigation on the long-term evolution of the Lonquimay volcano storage zones.

4.3 Volcanic hazard and risk reduction

This contribution reports that 17 tephra deposits formed during the last c. 5.5 ky at Lonquimay volcano, increasing the knowledge on the explosive behaviour of this volcanic complex. This number a 3-fold of the previously recognised tephra deposits for the same period by Gilbert et al. (2014). To understand how their incorporation affects the eruptive recurrence and probability of future eruptions, we follow the approach of Gilbert et al. (2014).

These authors assume that all the 22 tephra deposits in the <11 ka geological record represent single eruptions and consider another 5 historical eruptions ("extended record"). They also assume that all the tephras were produced by VEI=3 events. The resulting probabilities of at least one VEI $\geq$ 3 within 100 years after 2011 is 20-50%. Under the same assumptions, the same probability rises to 27-61% by incorporating our deposits. This range of probabilities accounts for the geological and extended records applying both Poisson and Log-logistic distributions (De la Cruz-Reyna, 1991; Mendoza-Rosas and De la Cruz-Reyna, 2008). These models approach to 100% probabilities after 400-600 years (Supplementary Material 6). In terms of eruption style, 89% tephra deposits represent fallout events, and 12% are PDCs. Airfall tephra is mainly dispersed east-southeast over inhabited areas (e.g., Lonquimay, Malalcahuello and small settlements along the Cordillera de Las Raíces). Additionally, 59% are dominated by scoria, 29% by pumice, and 12% by dense juvenile material. The scoria deposits are probably correlated to Strombolian and sub-Plinian parental eruptions, while the pumice is likely exclusively produced during sub-Plinian events (Fig. 12). In this regard, emergency preparedness should incorporate tephra-tolerance engineering for roofs, water systems and road infrastructure plus response mechanisms for cleanup (Fig. 12). Plans should involve health protection, shelter and evacuation for humans and animals, with special focus on environmental pollution monitoring. Considering the investigated PDC deposits are distributed towards the south and southeast, we confirm burial susceptibility at Malalcahuello and the Corralco Ski facilities, as previously envisaged by Naranjo et al. (2000). Given this context and the increasing amenity migration to the area (Vergara-Pinto et al., 2024), we advocate for more comprehensive territorial planning. This planning should foster dialogue among decision-makers, local communities, and newcomers about the associated risks. It is essential that individuals considering residence in high-risk zones—such as ravines and valleys near the volcano—have access to accurate, specialised information. This would enable them to make informed, responsible choices and, ideally, avoid settling in areas with clear evidence of recent pyroclastic density current activity. Finally, our research underscores the necessity of integrating community concerns and uncertainties into ongoing and future hazard research at Lonquimay volcano, as well as in other volcanic regions in the Southern Andes. This principle may improve the understanding of the needs and gaps in communities at risk, ultimately leading to more effective risk reduction strategies and improved preparedness measures in the face of volcanic hazards.

5 Conclusions

We carried out a first comprehensive study of the middle-to-late Holocene tephra sequences outcropping east of the Lonquimay-Tolguaca Volcanic Complex, which last erupted in 1988-1990. The motivation behind the case study lay primarily in the interest of the local community of Malalcahuello in the eruptive record they observe daily in the landscape, on the roads and in their homes, which raises questions and concerns like those of volcanological research (i.e., eruptive styles, types of products, time scales, among others).

We therefore integrate some of their questions into the study and offer new stratigraphic observation, several new isopach maps of tephra falls and distribution maps of PDCs, plus a general characterization of the geochemistry and mineralogy of these tephra deposits. In doing so, our research involved analyses at different scales, from field data collection to petrological investigation of pyroclasts.

We identified, at least, 17 tephra deposits within the last. *ca.* 5.5 ky by carrying out proximal-to-medial (2–15 km from the central crater) tephrostratigraphy. This record increases the probability of at least one VEI ≥ 3 to 27-61% within the next 100 years. The textural features of juvenile products indicate a dominant Strombolian to sub-Plinian eruption style. Moreover, we interpret that these eruptions are primarily fed from ~2 to ~7.5 kbar (~8 to ~30 km depth). The magmas are thermally bimodal but span a wide compositional range from basaltic to dacitic, and undergo fractionation and likely, interaction and mixing in a recharge-driven plumbing system. These additions will provide relevant information for updated hazard mapping, more accurate eruptive scenarios and, ultimately, disaster risk reduction by integrating community-based scientific questions into volcanological research.

Acknowledgements
We would like to thank Corporación Nacional Forestal for providing us with access to the Malalcahuello National Reserve. FV and JE thank the residents for their valuable insights and questions about volcanic behaviour and hazards. FC acknowledges funding from the Deutsche Forschungs-gemeinschaft (DFG -German Research Foundation) through the project number 457579444 (CA 2743/1-1). AC acknowledges Fondecyt Regular 1211869.

References

- Ágreda-López, M., Parodi, V., Musu, A., Jorgenson, C., Carfì, A., Mastrogiovanni, F., Caricchi, L., Perugini, D., Petrelli, M. (2024). Enhancing machine learning thermobarometry for clinopyroxene-bearing magmas. Computers & Geosciences, 193, 105707.
- Alegría, C., Vergara-Pinto, F. (2024). Living in-between: Implications of local risk perceptions for the management of future eruptions at the Calbuco and Osorno volcanoes (Ensenada, Chile). Andean Geology, 51(1), 63-85.
- Alfano, F., Bonadonna, C., Gurioli, L. (2012). Insights into eruption dynamics from textural analysis: the case of the May, 2008, Chaitén eruption. Bull Volcanol 74, 2095–2108. https://doi.org/10.1007/s00445-012-0648-3
- Arzilli, F., Morgavi, D., Petrelli, M., Polacci, M., Burton, M., Di Genova, D., La Spina, L., La Spina, G., Hartley, M., Romero, J.E., Fellowes, J., Díaz-Alvarado, J., Perugini, D. (2019). The unexpected explosive sub-Plinian eruption of Calbuco volcano (22–23 April 2015; southern Chile): Triggering mechanism implications. J Volcanol Geotherm Res, 378, 35-50.
- Barclay, J., Rutherford, M.J., Carroll, M.R., Murphy, M.D., Devine, J.D., Gardner, Sparks, R.S.J. (1998) Experimental phase equilibria constraints on pre-eruptive storage conditions of the Soufriere Hills magma. Geophysical Research Letters, 25(18), 3437-3440.

- Besoaín, E., Sepúlveda, G., Sadzawka, A. (1992). La erupción del volcán Lonquimay y sus efectos en la agricultura. Agricultura Técnica 52(4): 354-358.
- Blundy, J., Cashman, K. (2008). Petrologic reconstruction of magmatic system variables and processes. Rev Mineral Geochem 69(1):179–239
- Bonadonna, C., Costa, A. (2012). Estimating the volume of tephra deposits: a new simple strategy. Geology, 40(5), 415-418. https://doi.org/10.1130/ G32769.1
- Bonadonna, C., Pistolesi, M., Biass, S., Voloschina, M., Romero, J., Cappola, D., Folch, A., D'Auria, L., Martin-Lorenzo, A., Dominguez, L., Pastore, C., Reyes Hardy, M-P., Rodríguez, F. (2022) Physical characterization of long-lasting hybrid eruptions: the 2021 Tajogaite eruption of Cumbre Vieja (La Palma, Canary Islands). J Geophys Res: Solid Earth, 127(11): e2022JB025302.
- Büttner, R., Dellino, P., Zimanowski, B. (1999). Identifying magma water interaction from the surface features of ash particles. Nature 401:688–690
- Cashman, K.V., Sparks, R.S.J., Blundy, J.D. (2017). Vertically extensive and unstable magmatic systems: a unified view of igneous processes. Science, 355(6331), eaag3055.
- Cembrano, J., Lara, L. (2009). The link between volcanism and tectonics in the southern volcanic zone of the Chilean Andes: A review. Tectonophysics, 471(1-2), 96-113.
- Cioni, R., D'Oriano, C., Bertagnini, A. (2008). Fingerprinting ash deposits of small-scale eruptions by their physical and textural features. J Volcanol Geotherm Res 177(1):277–287
- Cole, P.D., Barclay, J., Robertson, R.E.A., Mitchell, S., Davies, B.V., Constantinescu, R., Sparks, R.S.J., Aspinall, A., Stinton, A. (2024). Explosive sequence of La Soufrière, St Vincent, April 2021: insights into drivers and consequences via eruptive products. Geological Society, London, Special Publications, 539(1), 81-106.
- Cutler, K.S., Cassidy, M., & Blundy, J.D. (2024). Plagioclase-saturated melt hygrothermobarometry and plagiolase-melt equilibria using machine learning. Geochem Geophys Geosyst, 25, e2023GC011357
- Daggitt, M.L., Mather, T.A., Pyle, D.M., Page, S. (2014). AshCalc-a new tool for the comparison of the exponential, power-law and Weibull models of tephra deposition. J Applied Volcanol, 3, 7. https://doi.org/10.1186/2191- 5040-3-7
- De la Cruz-Reyna, S. (1991). Poisson-distributed patterns of explosive eruptive activity. Bull Volcanol, 54(1): 57-67.
- Dellino, P., Liotino, G. (2002). The fractal and multifractal dimension of volcanic ash particles contour: a test study on the utility and volcanological relevance. J Volcanol Geotherm Res, 113(1-2): 1-18.
- Fabbrizio, A., Špillar, V. (2020). Methodology to derive well-calibrated thermometers: a new glass-composition geothermometer for olivine-bearing glassy samples at one atmospher. Ann Geophys, 63(4): DM436-DM436.
- Fierstein, J., Nathenson, M. (1992). Another look at the calculation of fallout tephra volumes. Bull Volcanol, 54(2): 156-167. https:// doi.org/10.1007/BF00278005.
- Fisher, R.V., Schmincke, H-U. (1984). Pyroclastic Rocks. Springer-Verlag, Berlin, p 472
- Fontijn, K., Rawson, H., Van Daele, M., Moernaut, J., Abarzúa, A. M., Heirman, K., Bertrand, S., Pyle, S., Mather, T.A., De Batist, M., Naranjo, J.A., Moreno, H. (2016).

Synchronisation of sedimentary records using tephra: A postglacial tephrochronological model for the Chilean Lake District. Quat Sci Rev, 137, 234-254.

- Gardner, C., Cashman K., Neal, C. (1998). Tephra-fall deposits from the 1992 eruption of Crater Peak, Alaska: implications of clast textures for eruptive processes. Bull Volcanol 59, 537–555. https://doi.org/10.1007/s004450050208
- Gertisser, R., Keller, J. (2003). Temporal variations in magma composition at Merapi Volcano (Central Java, Indonesia): magmatic cycles during the past 2000 years of explosive activity. J Volcanol Geotherm Res, 123(1-2): 1-23.
- Gilbert, D., Freundt, A., Kutterolf, S., Burkert, C. (2014). Post-glacial time series of explosive eruptions and associated changes in the magma plumbing system of Lonquimay volcano, south central Chile. Int J Earth Sci, 103: 2043-2062.
- Heiken, G. (1972) Morphology and petrography of volcanic ashes. Geol Soc Am Bull 83(7):1961-1988.
- Hickey-Vargas, R., Holbik, S., Tormey, D., Frey, F. A., Moreno, H. (2016). Basaltic rocks from the Andean Southern Volcanic Zone: Insights from the comparison of along-strike and small-scale geochemical variations and their sources. Lithos 258: 115-132.
- Hogg, A.G., Heaton, T.J., Hua, Q., Palmer, J.G., Turney, C.S.M., Southon, J., Bayliss, A., Blackwe, Boswijk, G., Bronk Ramsey, C., Pearson, C., Petchey, F., Reimer, P., Reimer, R., Wacker, L. (2020). SHCal20 Southern Hemisphere calibration, 0-55,000 years cal BP. Radiocarbon 62. doi: 10.1017/RDC.2020.59
- Houghton, B., Carey, R.J. (2015). Pyroclastic fall deposits. In The Encyclopedia of Volcanoes (pp. 599-616). Academic Press.
- Houghton, B.F., Gonnermann, H.M. (2008). Basaltic explosive volcanism: constraints from deposits and models. Geochemistry 68(2): 117-140.
- Le Bas, M., Le Maitre, R., Streckeisen A, Zanettin B, IUGS Subcommission on the Systematics of Igneous Rocks (1986) A chemical classification of volcanic rocks based on the total alkali-silica diagram. J Petrol 27(3): 745-750.
- Lowe, D.J. (2011). Tephrochronology and its application: a review. Quat Geochron, 6(2), 107-153.
- Lowe, D.J., Alloway, B.V. (2014). Tephrochronology. In: Rink, W.J., Thompson, J. (Eds.), Encyclopedia of Scientific Dating Methods. Springer, Netherlands, 1–26.
- Macomber, T. (2015). The evolution of a monogenetic eruption: Navidad Eruption, Lonquimay Volcano, Chile (Master dissertation, State University of New York at Buffalo).
- Martel, C., Pichavant, M., Balcone-Boissard, H., Boudon, G. (2021). Syn-Eruptive Conditions of the AD 1530 Sub-Plinian Eruption of La Soufrière of Guadeloupe (Lesser Antilles). Front Earth Sci 9: 686342. doi: 10.3389/feart.2021.686342.
- Melekhova, E., Annen, C., Blundy, J. (2013). Compositional gaps in igneous rock suites controlled by magma system heat and water content. Nat Geosci, 6(5), 385-390.
- Mendoza-Rosas, A.T., De la Cruz-Reyna, S. (2008). A statistical method linking geological and historical eruption time series for volcanic hazard estimations: applications to active polygenetic volcanoes. J Volcanol Geoth Res 176(2):277–290. doi:10.1016/j.jvolgeores.2008.04.005
- Moreno, H., Gardeweg, M. (1989). La erupción reciente en el complejo volcánico Lonquimay (Diciembre 1988), Andes del Sur. Rev Geol Chile, 16(1): 93-117.

- Moreno, H., Naranjo, J.A., Polanco, E. (2023). Geología del Complejo Volcánico Lonquimay-Tolguaca, regiones del Biobío y de La Araucanía. Servicio Nacional de Geología y Minería, Carta Geológica de Chile, Serie Geología Básica 219: 53 p., 1 mapa escala 1:50.000. Santiago
- Morimoto, N. (1989). Nomenclature of pyroxenes. The Canadian Mineralogist 27, Part 1: 143-156.
- Naranjo, J.A., Moreno, H., Gardeweg, M. (1991). Erupción de 1988-1990 del volcán Lonquimay, Andes del Sur (38° 20'S), Chile. In Congreso Geológico chileno. 6 (pp. 445-448).
- Naranjo, J.A., Sparks, R.S.J., Stasiuk, M.V., Moreno, H., Ablay, G.J. (1992). Morphological, structural and textural variations in the 1988–1990 andesite lava of Lonquimay Volcano, Chile. Geol Mag, 129(6): 657-678.
- Naranjo, J.A., Moreno, H., Polanco, E., Young, S. (2000). Mapa de peligros de los volcanes del Alto Biobío, Regiones del Biobío y de La Araucanía. Servicio Nacional de Geología y Minería, Documentos de Trabajo 15, 1 mapa escala 1 100.000. Santiago.
- Neave, D.A., Putirka, K.D. (2017). A new clinopyroxene-liquid barometer, and implications for magma storage pressures under Icelandic rift zones. Am Mineral 102(4): 777-794.
- Newhall, C.G., Self, S. (1982). The volcanic explosivity index (VEI) an estimate of explosive magnitude for historical volcanism. J Geophys Res: Oceans, 87(C2): 1231-1238.
- Nimis, P. (1995). A clinopyroxene geobarometer for basaltic systems based on crystal-structure modeling. Contrib Mineral Petrol, 121: 115-125.
- Nimis P, Ulmer P (1998) Clinopyroxene geobarometry of magmatic rocks Part 1: An expanded structural geobarometer for anhydrous and hydrous, basic and ultrabasic systems. Contrib Mineral Petrol 133(1): 122-135.
- Peccerillo, A., Taylor, S.R. (1976). Geochemistry of Eocene calc-alkaline volcanic rocks from the Kastamonu area, northern Turkey. Contrib Mineral Petrol, 58: 63-81.
- Pistolesi, M., Cioni, R., Bonadonna, C., Elissondo, M., Baumann, V., Bertagnini, A., Chiari, L., Gonzales, R., Rosi, M., Francalanci, L. (2015). Complex dynamics of small-moderate volcanic events: the example of the 2011 rhyolitic Cordón Caulle eruption, Chile. Bull Volcanol, *77*(1): 3.
- Poblete, M., Castruccio, A., Larrea, P., Cáceres, F., Romero, J.E., Bustamante, O. (2025). Pre-eruptive conditions of Mid-to-Late Holocene eruptions from Lonquimay Volcanic Complex, Southern Andes of Chile. J Volcanol Geoth Res, 108425.
- Polacci, M., Corsaro, R.A., Andronico, D. (2006). Coupled textural and compositional characterization of basaltic scoria: Insights into the transition from Strombolian to fire fountain activity at Mount Etna, Italy. Geology, 34(3): 201-204.
- Polanco, E. (1998). Volcanismo Explosivo Postglacial de la Cuenca del Alto Biobío, Andes del Sur (37450–38300). Master, Universidad de Chile, Santiago de Chile.
- Polanco, E. (2010). Volcanoestratigrafía, geoquímica y peligro volcánico del volcán Lonquimay (38º30'S), Andes del Sur (Chile). Universidad de Barcelona, Barcelona. 256 p.
- Putirka, K.D. (2008). Thermometers and barometers for volcanic systems. Reviews in mineralogy and geochemistry 69(1): 61-120.

- Pyle, D.M. (1989). The thickness, volume and grainsize of tephra fall deposits. Bull Volcanol 51(1): 1-15. https://doi.org/10.1007/ BF01086757
- Re, G., Corsaro, R.A., D'Orianoa, C., Pompilio, M. (2021). Petrological monitoring of active volcanoes: a review of existing procedures to achieve best practices and operative protocols during eruptions. J Volcanol Geotherm Res 419:107365.
- Roeder, P.L., Emslie, R. (1970). Olivine-liquid equilibrium. Contrib Mineral Petrol 29(4): 275-289.
- Romero, J.E., Alloway, B.V., Gutiérrez, R., Bertín, D., Castruccio, A., Villarosa, G., Schipper, I.C., Guevara, A., Bustillos, J., Pisello, A., Daga, R., Montiel, M., Gleeman, E., González, M., Morgavi, D., Ribeiro Guevara, S., Mella, M. (2021). Centennial-scale eruptive diversity at Volcán Calbuco (41.3 S; Northwest Patagonia) deduced from historic tephra cover-bed and dendrochronologic archives. J Volcanol Geotherm Res 417: 107281.
- Romero, J.E., Douillet, G.A., Vallejo Vargas. S., Bustillos, J., Troncoso, L., Díaz-Alvarado, J., Ramón, P. (2017). Dynamics and style transition of a moderate, Vulcanian-driven eruption at Tungurahua (Ecuador) in February 2014: pyroclastic deposits and hazard considerations. Solid Earth 8(3): 697-719.
- Romero, J.E., Gallardo, D.I., Gaitán, J.J., Swanson, F., Sánchez, F., Saavedra, M., Zambrano, N., Buckland, H., Rodríguez, I. (2024b). The 2011-2012 Puyehue-Cordón Caulle (Southern Andes) tephra deposit: influence of the number of field measurements on isopach drawing and volume estimate. Est Geol, 80(1): 1075. https://doi.org/10.3989/egeol.45173.1075
- Romero, J.E., Vergara-Pinto, F., Forte, P., Ovalle, J., Sánchez, F. (2024a). The Andean Southern Volcanic Zone: a review on the legacy of the latest volcanic eruptions. Andean Geology 51 (2): 379- 412. https://doi.org/10.5027/andgeoV51n2-3681
- Romero, J. E., Cáceres, F., Guevara, A., Vergara-Pinto, F., Boschetty, F., Burton, M., Polacci, M., Morgado, E., Contreras, C., Vera, F., Aqueveque, O., Quilodrán, A., Amigo, Á. (2025). Magma recharge and reheating driving the 2021–2023 tephra emissions of Villarrica volcano, southern Andes. Bull Volcanol, 87(6): 1-18.
- Romero, J.E., Morgado, E., Pisello, A., Boschetty, F., Petrelli, M., Cáceres, F., Alam, M.A., Polacci, M., Palma, J.L., Arzilli, F., Vera, F., Gutiérrez, R., Morgavi, D. (2023). Pre-eruptive Conditions of the 3 March 2015 Lava Fountain of Villarrica Volcano (Southern Andes). Bull Volcanol, 85: 2. https://doi.org/10.1007/s00445-022-01621-0.
- Ross, P.S., Dürig, T., Comida, P.P., Lefebvre, N., White, J.D., Andronico, D., Thivet, S., Eyechenne, J., Gurioli, L. (2022). Standardized analysis of juvenile pyroclasts in comparative studies of primary magma fragmentation; 1. Overview and workflow. Bulletin Volcanol, 84: 1-29.
- Salas, P., Ruprecht, P., Hernández, L., Rabbia, O. (2021). Out-of-sequence skeletal growth causing oscillatory zoning in arc olivines. Nat Comm, 12(1): 4069.
- Smith, R., Sammonds, P.R., Kilburn, C.R. (2009). Fracturing of volcanic systems: Experimental insights into pre-eruptive conditions. Earth Planet Sci Lett, 280(1-4): 211-219.
- Stern, C.R. (2004). Active Andean volcanism: its geologic and tectonic setting. Rev Geol Chile, 31 (2): 161-206.

- Stern, C.R., López-Escobar, L., Moreno, H., Clavero, J., Naranjo, J.A., Parada, M.A., Skewes, M.A. (2007). Chilean Volcanoes. In The Geology of Chile (Moreno T, Gibbons W, editors). Geol Soc London, Chapter 5: 149-180.
- Streck, M.J. (2008). Mineral textures and zoning as evidence for open system processes. Rev Mineral Geochem, 69(1): 595-622.
- Tassara, A., Echaurren, A. (2012). Anatomy of the Andean subduction zone: three-dimensional density model upgraded and compared against global-scale models. Geophys J Int, 189(1): 161-168.
- Thornber, C.R., Huebner, J.S. (1985). Dissolution of olivine in basaltic liquids: experimental observations and applications. Am Mineral 70(9-10): 934-945.
- Tognetti, R., Lombardi, F., Lasserre, B., Battipaglia, G., Saurer, M., Cherubini, P., Marchetti, M. (2012). Tree-ring responses in Araucaria araucana to two major eruptions of Lonquimay Volcano (Chile). Trees, 26, 1805-1819.
- Vergara-Pinto, F., Marín, A. (2023). Stratigraphy of volcanic memory: Sociocultural dimensions of volcanic risk in the southern Andes, Chile. Contingencies Crisis Manag, 31(4): 1018-1033.
- Vergara-Pinto, F., O'grady, N., Fredriksen, A., Romero, J.E., Marchant, C., Walshe, R., Donovan, A., Morin, J., Szlam, M. (2024). How residents and volcanoes co-produce risk knowledge: Ways of knowing and affective attunement to the rhythms of Lonquimay volcano, Chile. J Volcanol Geotherm Res, 108180.
- Walker, G.P.L. (1971). Grain-size characteristics of pyroclastic deposits. J Geol 79:696–714
- Walshe, R., Morin, J., Donovan, A., Vergara-Pinto, F., Smith, C. (2023). Contrasting memories and imaginaries of Lonquimay volcano, Chile. Int J Disaster Risk Reduct, 97: 104003.
- Wang, X., Hou, T., Wang, M., Zhang, C., Zhang, Z., Pan, R., Marxer, F., Zhang, H. (2021). A new clinopyroxene thermobarometer for mafic to intermediate magmatic systems, Eur J Mineral 33: 621–637, https://doi.org/10.5194/ejm-33-621-2021
- Weber, G., Blundy, J. (2024). A machine learning-based thermobarometer for magmatic liquids. J Petrol, 65(4): egae020
- Weber, G., Simpson, G., Caricchi, L. (2020). Magma diversity reflects recharge regime and thermal structure of the crust. Sci Rep, 10(1): 11867.
- Weller, D., Colombier, M., Cáceres, F., Vasseur, J., Dingwell, D.B., Scheu, B. (2024). Confocal Scanning Laser Microscopic (CSLM) characterization of volcanic rocks. J Volcanol Geotherm Res, 446: 107992.
- Wieser, P.E., Kent, A.J., Till, C.B., Donovan, J., Neave, D.A., Blatter, D.L., Krawczynski, M.J. (2023). Barometers behaving Badly I: Assessing the influence of analytical and experimental uncertainty on clinopyroxene thermobarometry calculations at crustal conditions. J Petrol, 64(2), egac126.
- Wieser, P., Petrelli, M., Lubbers, J., Wieser, E., Ozaydin, S., Kent, A. and Till, C. (2022) “Thermobar: An open-source Python3 tool for thermobarometry and hygrometry”, Volcanica, 5(2), pp. 349–384. doi: 10.30909/vol.05.02.349384.
- Zellmer, G.F., Freymuth, H., Cembrano, J.M., Clavero, J.E., Veloso, E.A., Sielfeld, G.G. (2014). Altered mineral uptake into fresh arc magmas: insights from U–Th isotopes of samples from Andean volcanoes under differential crustal stress regimes. Geol Soc Spec Pub, 385(1): 185-208.

- Zimanowski, B., Büttner, R., Dellino, P., White, J.D., Wohletz, K.H. (2015). Magma–water interaction and phreatomagmatic fragmentation. In The encyclopedia of volcanoes (pp. 473-484). Academic Press.

Figure captions

Fig. 1: Location map of the Lonquimay-Tolguaca Volcanic Complex (LVC). The Liquiñe-Ofqui Fault Zone (LOFS) is based on Moreno et al. (2024), whereas vents including small eruptive centres (SECs) have been interpreted from the satellite image.

Fig. 2: Field observations of tephra deposits. Red lines represent stratigraphic unconformities, whereas white and black lines represent stratigraphic contacts. ULS, MLS and LLS correspond to the upper, middle, and lower Lonquimay tephra sequences, respectively (Gilbert et al., 2014). The names of some tephra deposits are indicated.

Fig. 3: Composite stratigraphy, with the maximum observed thicknesses, acronyms of pyroclastic units, available calibrated ages (CE=Christian Era; BP=Before present), and texture of juvenile material.

Fig. 4: Tephrostratigraphic correlation of Upper Lonquimay Sequence tephras between proximal and medial field sites (orange squares in the map). Control points are indicated as green circles. Samples are represented by red circles with a star at representative stratigraphic sections. The names of the correlated tephras are in bold italic. Thicknesses are measured in metres.

Fig. 5: Distribution of mid-to-late Holocene tephra fall and pyroclastic density current (PDC) deposits (central-right panel). Isopach maps (cm) for KM, AK and CU drawn from new field control points, and for NV modified from Naranjo et al. (1991). The lower right panel shows the regressions of thickness v/s square root of the area for the tephra fall deposits and their corresponding volumes.

Fig. 6: Backscattered electron images of representative pyroclast textures from groups 1 to 5 at different magnification scales (left axis). Sample codes and unit names are indicated at the upper horizontal axis. Components correspond to Pl=plagioclase, Ol=olivine, Px=pyroxene, Ox= Fe-Ti oxides, Ves=vesicles, and Gm=groundmass.

Fig. 7: Whole-rock (circles) and groundmass glass (open symbols) geochemistry (normalised, volatile free) of sampled pyroclastic products from the upper Lonquimay tephra sequence (ULS, mid-to-late Holocene) grouped by compositional clusters. ULS* and ULS** represent whole-rock and groundmass glass data reported in Polanco (1998) and Gilbert et al. (2014). **a)** Total alkali vs silica diagram of Le Bas (1986) and **b)** K_2O vs SiO_2 diagram (Peccerillo and Taylor, 1976). Letters represent: B=basalt, BA=basaltic andesite, A=andesite, BTA=basaltic trachyandesite, TA=trachyandesite, D=dacite, T=trachyte, and R=rhyolite. **c)** K_2O/TiO_2 vs SiO_2 diagram based on Gilbert et al. (2014). The circles indicate the distinctive compositional fields. **d)** FeO_T/MgO vs. CaO/Al_2O_3 diagram, indicating the different crystallisation trends and mineral phases, and a possible trend of mixing. FeO_T is the total iron reported by the microprobe as FeO for groundmass glasses, and as Fe_2O_3 by the

XRF. **g)** Stratigraphic variation of whole-rock SiO_2 and MgO from younger (upper, Navidad) to older (lower, La Negra).

Fig. 8: Mineral compositions for the different groups of tephras analysed in this work. a) Ternary diagram for plagioclase feldspars. b) normalised histograms for forsterite mol.%. c) Pyroxene ternary diagram (Morimoto, 1989). Existing data refers to Polanco (2010) and Macomber (2015).

Fig. 9: Violin-dotplot of thermobarometry results for Lonquimay magmas. Each dot represents a pressure or temperature estimate, while "violins" in the background show the kernel density distribution. The colour coding reflects the erupted magma composition: basalt (red), basaltic andesite (orange), andesite (green), and dacite (blue). a) Temperature estimates using olivine-liquid pairs (Putirka, 2008), clinopyroxene-liquid and clinopyroxene-only (Ágreda López et al., 2024), glass- and whole rock-assemblage thermometry (Weber and Blundy, 2024). b) Pressure and corresponding depth estimates with constant density of 2700 kg m^{-3} using the methods as in a).

Fig. 10: Summary of most frequent explosive eruption styles and their related characteristics during the last ca. 5.5 ky, based on the findings of this study. Some mitigation measures for volcanic risk reduction in rural areas are suggested.

Supplementary materials

- **Supplementary material 1:** Examples of residents' questions and concerns about LTVC threats, which inspired the study.
- **Supplementary material 2:** Calibrated ages of radiocarbon dates previously available in the literature. *From Polanco (1998) and **Gilbert et al. (2014).
- **Supplementary material 3:** Electron microprobe geochemical data of glass and mineral phases of the Lonquimay tephras analysed in this study.
- **Supplementary material 4:** Mineral-melt and Melt-Assemblage datasets used for geothermometry and geobarometry in this study.
- **Supplementary material 5:** Results of the plagioclase-saturated melt hygrothermobarometry (Cutler et al., 2024) for groundmass glass compositions reported in this study.
- **Supplementary material 6:** Results of the probabilistic assessment for future VEI≥3 eruptions at the Lonquimay-Tolguaca volcanic complex considering the updated stratigraphy available in this contribution.

Supplementary figures

- **Supplementary Figure 1:** Malalcahuello village (a), where interviews were conducted with some residents in various contexts (b-e), addressing their uncertainties about volcanic hazards. Simultaneously, tephra samples were collected in the vicinity of the volcano (f).

- **Supplementary Figure 2:** Harker diagrams for major element compositions on whole rock analyses of 16 collected samples for this study.
- **Supplementary Figure 3:** Disequilibrium textures in basaltic and basaltic andesite samples of Lonquimay volcano. **a**) skeletal texture in a euhedral olivine phenocryst in sample BMNV89. **b**) skeletal growth of olivine microlites in sample MXNV89 (red circles). **c**) and **d**) spongy cellular texture (red arrows) and embayment in plagioclase phenocrysts in sample LQ18-B, respectively. Ol=olivine; Pl=plagioclase; Ox=oxide; Gls=glass; Gms=groundmass.

Highlights

- We describe fifteen tephra deposits of the Lonquimay-Tolguaca Volcanic Complex (LTVC; Southern Chile) for the last 5.5 ka.
- These deposits mostly comprise Strombolian to Subplinian eruption, with a maximum VEI 3 and volumes of 10^7 m^3.
- Eruptive products range from basalts to dacites sourced from regions ~2 to ~7.5 kbar depth.
- Data responds to questions and concerns of the local community regarding the eruptive activity and future scenarios of the LTVC.

Figure 1

Click here to access/download;Figure;Fig. 1.jpg

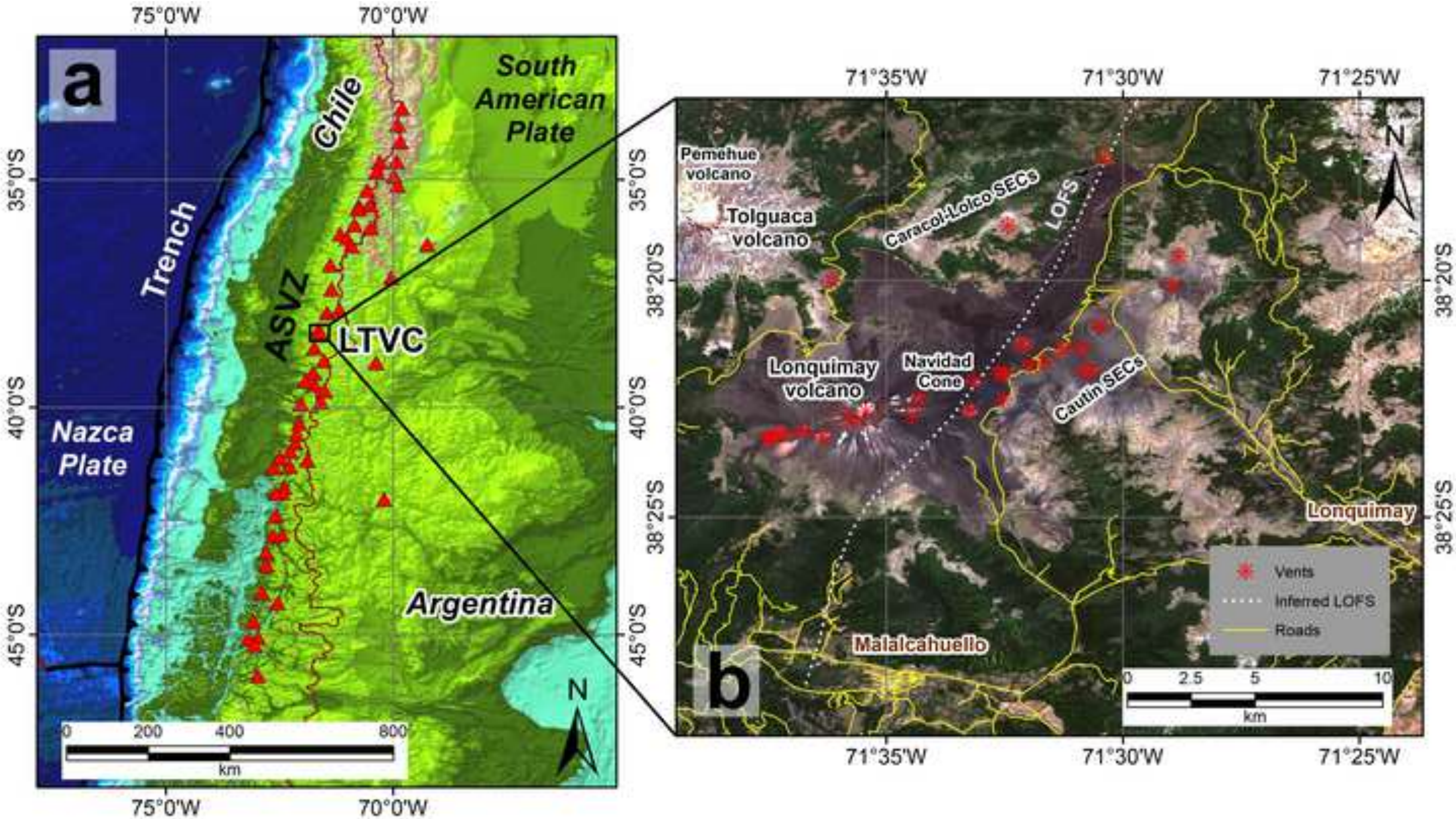

Figure 2

Click here to access/download;Figure;Fig. 2.jpg

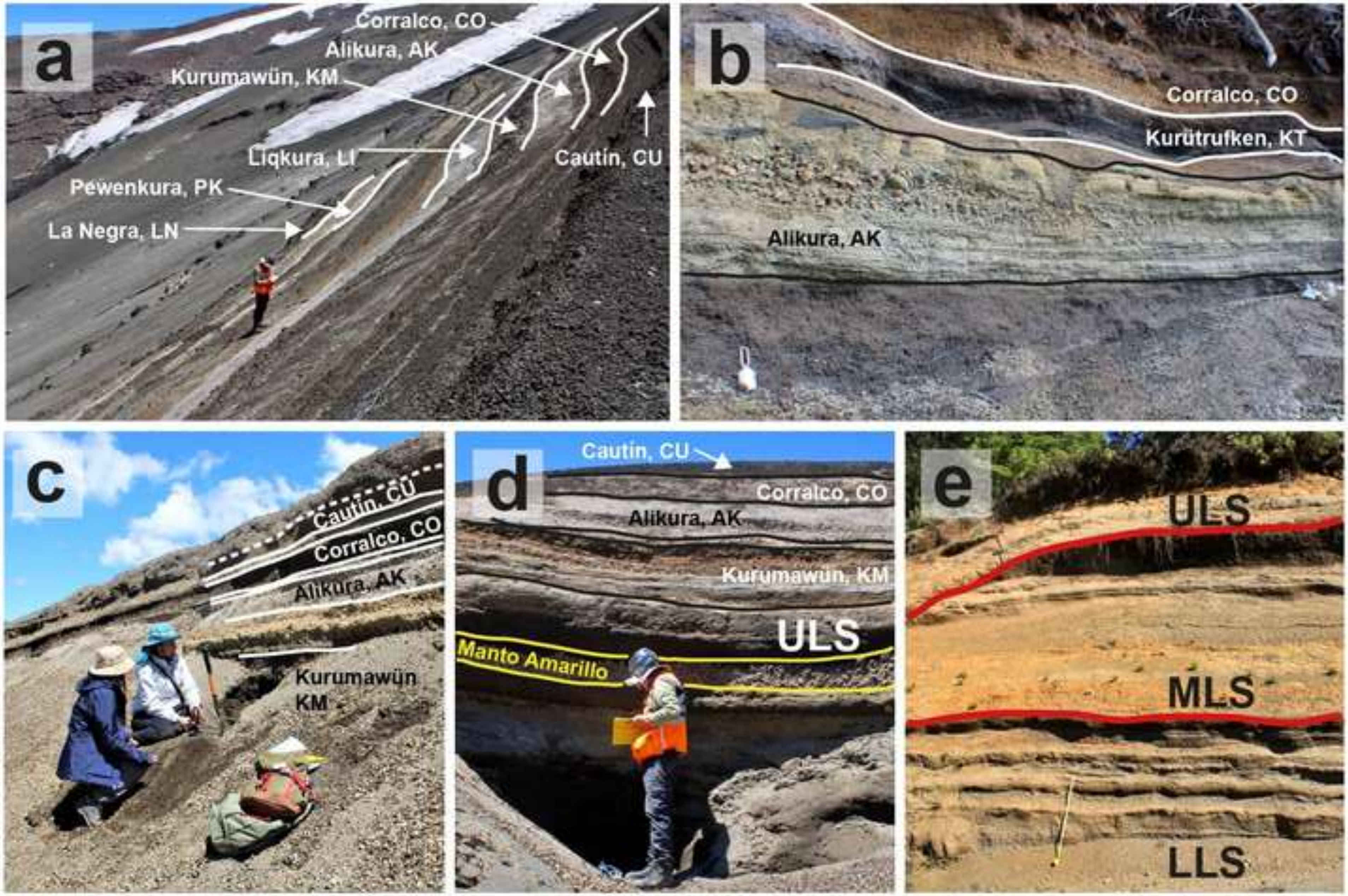

Figure 3 Click here to access/download;Figure;Fig. 3.jpg

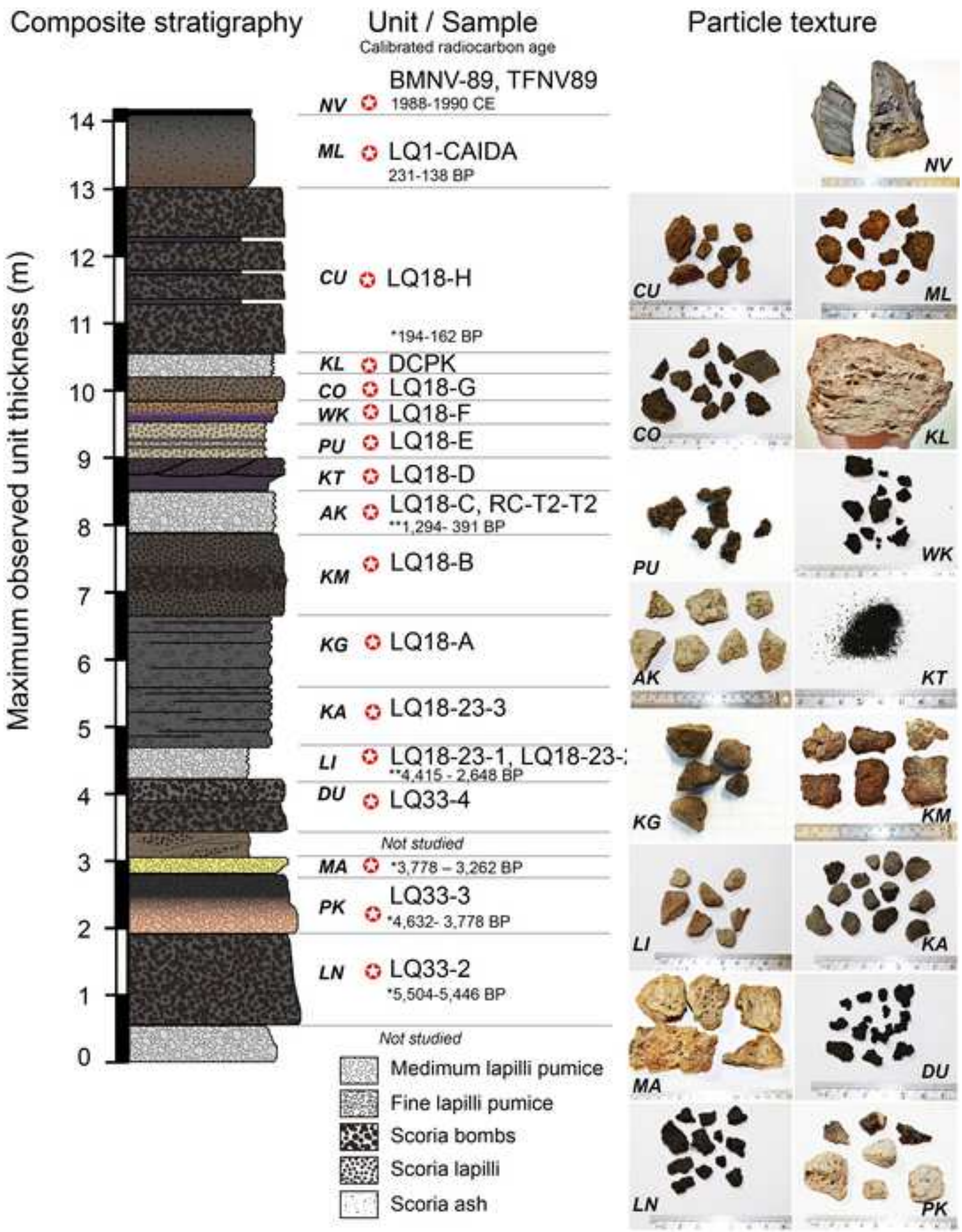

Figure 4 Click here to access/download;Figure;Fig. 4.jpg

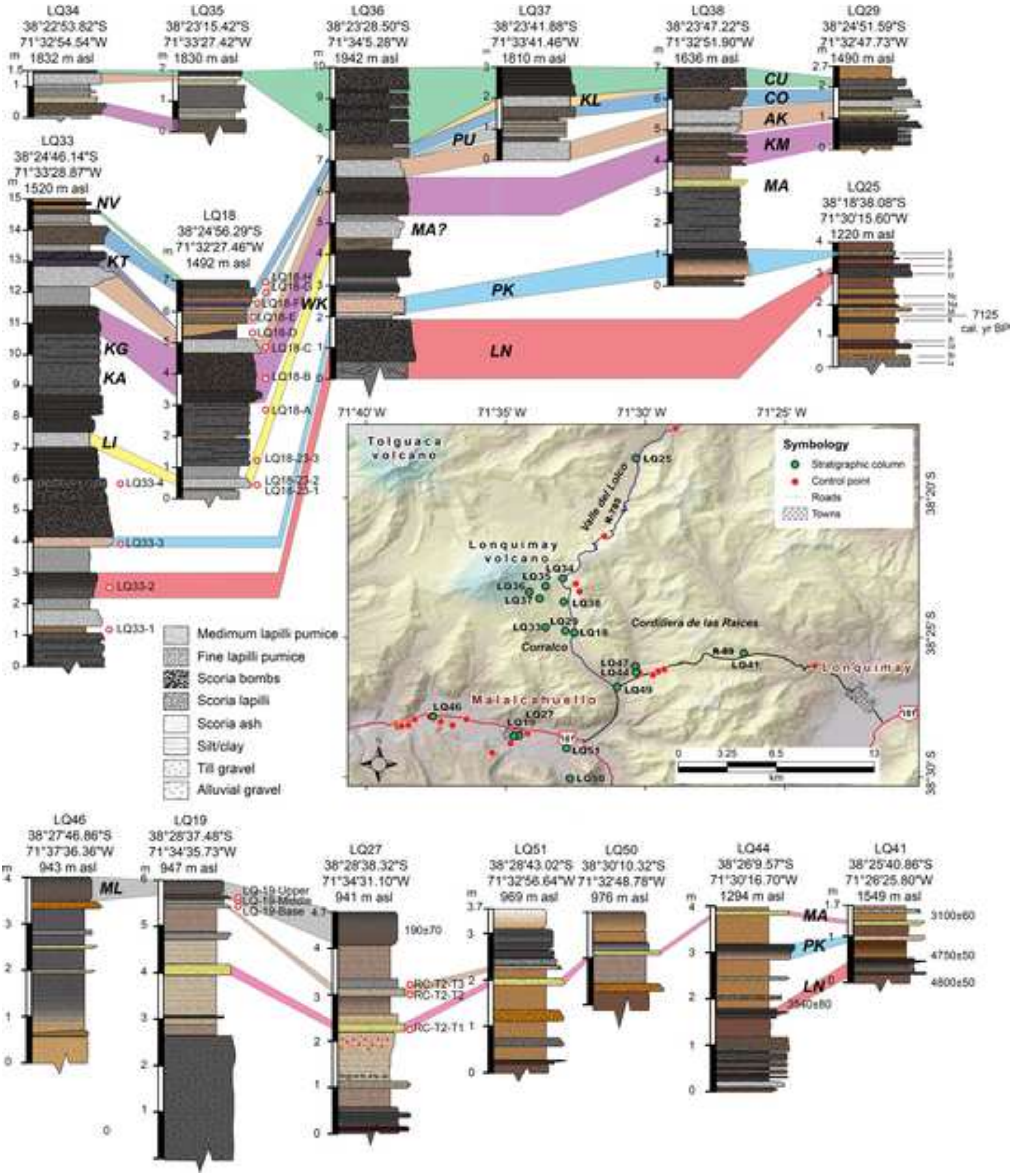

Figure 5

Click here to access/download;Figure;Fig. 5.jpg

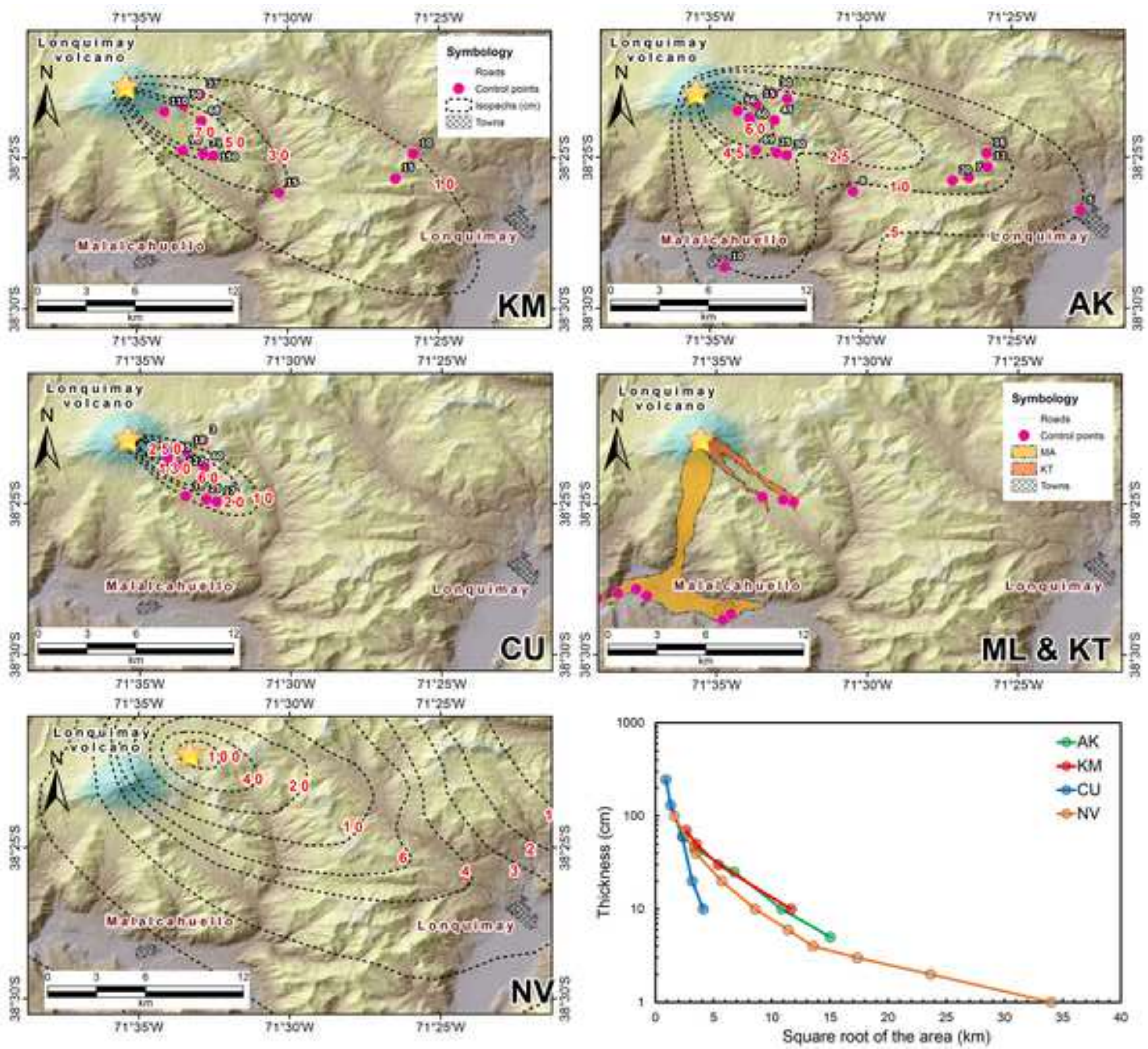

Figure 6

Click here to access/download;Figure;Fig. 6.jpg

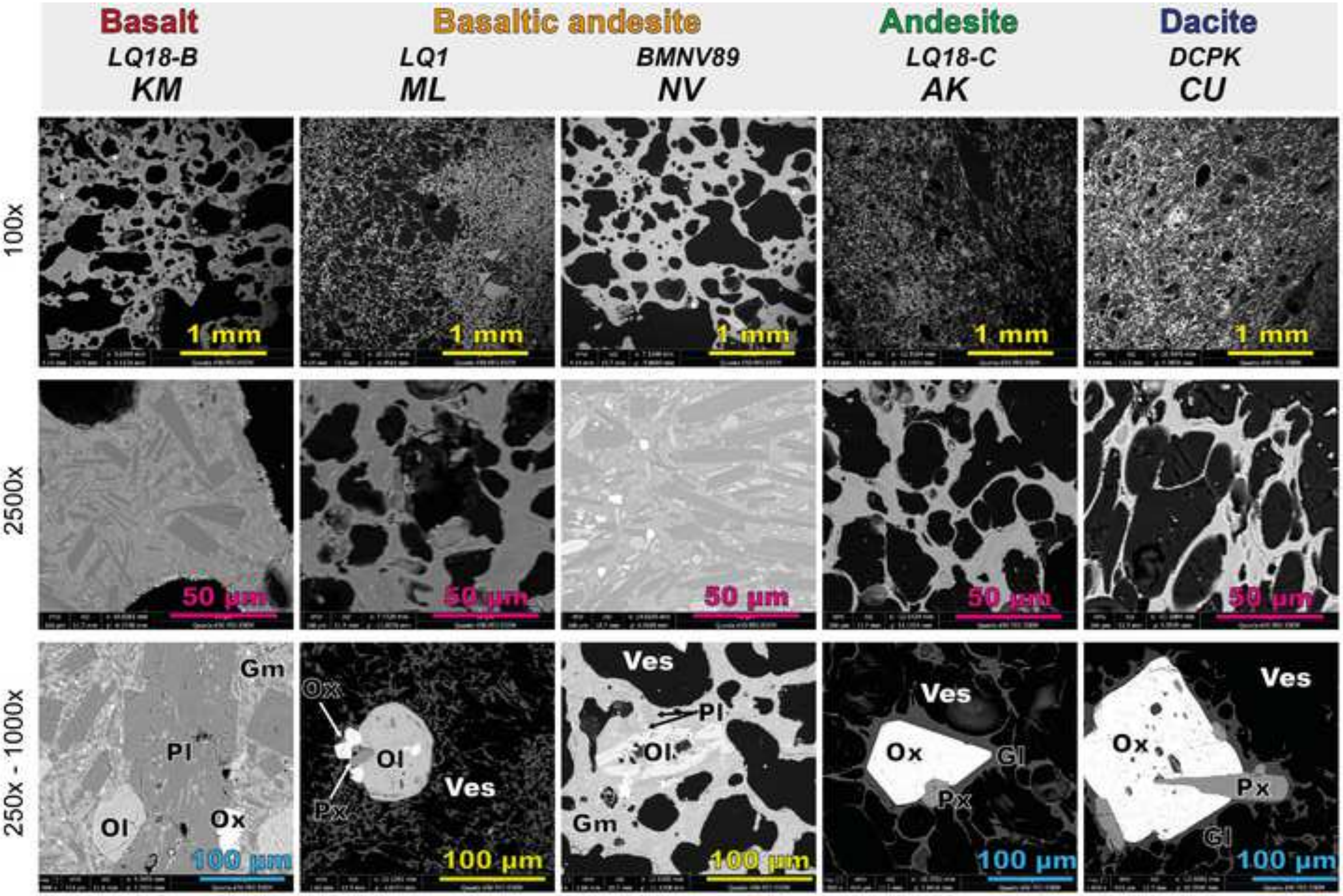

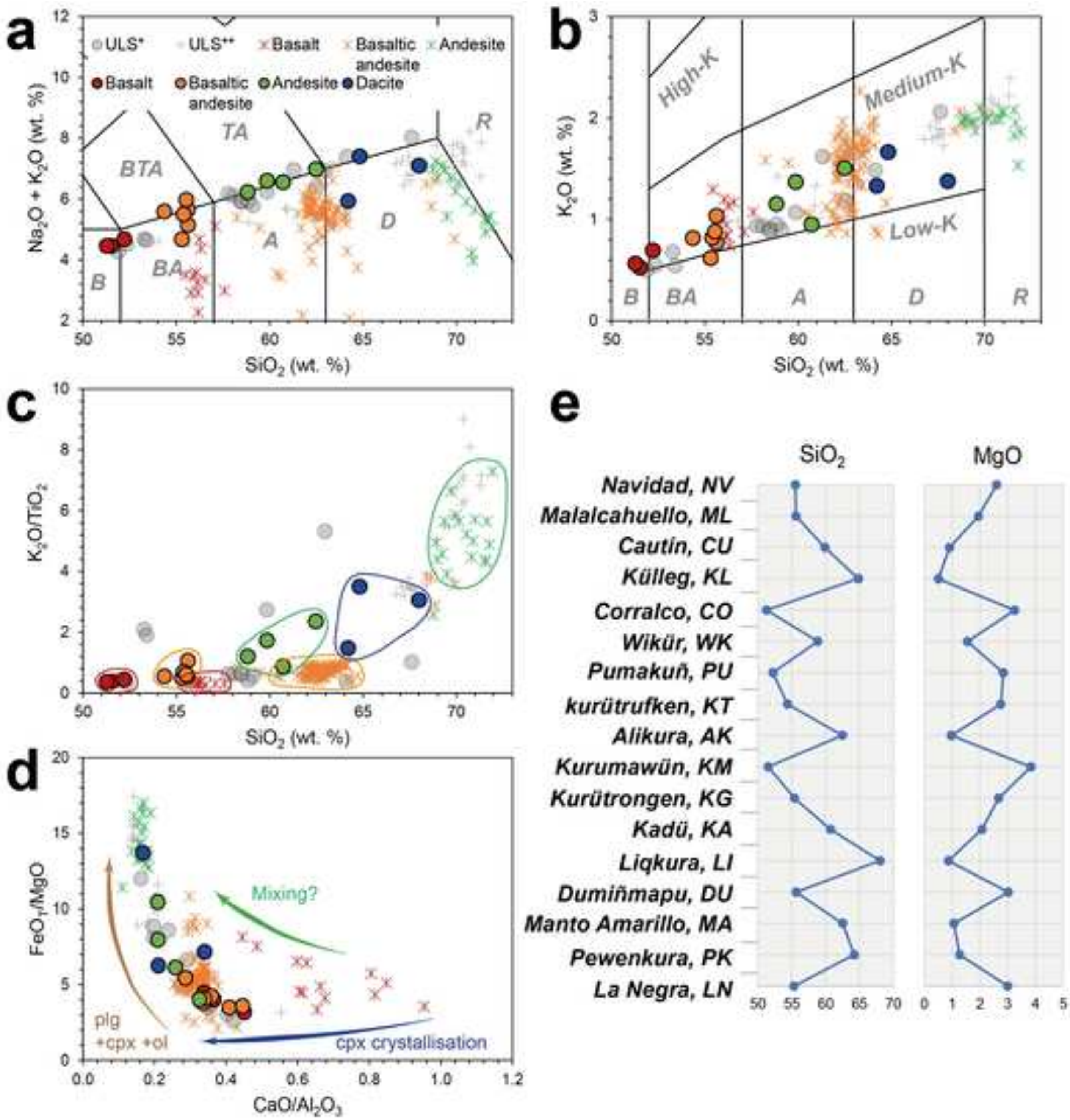
a
ULS*
ULS**
Basalt
Basaltic andesite
Andesite
Basalt
Basaltic andesite
Andesite
Dacite
BTA
TA
R
B
BA
A
D
Na2O + K2O (wt. %)
SiO2 (wt. %)
b
High-K
Medium-K
Low-K
B
BA
A
D
R
K2O (wt. %)
SiO2 (wt. %)
c
K2O/TiO2
SiO2 (wt. %)
d
Mixing?
plg +cpx +ol
cpx crystallisation
FeOT/MgO
CaO/Al2O3
e
SiO2
MgO
Navidad, NV
Malalcahuello, ML
Cautín, CU
Külleg, KL
Corralco, CO
Wikür, WK
Pumakuñ, PU
kurütrufken, KT
Alikura, AK
Kurumawün, KM
Kurütrongen, KG
Kadü, KA
Liqkura, LI
Dumiñmapu, DU
Manto Amarillo, MA
Pewenkura, PK
La Negra, LN

Figure 8

Click here to access/download;Figure;Fig. 8.jpg

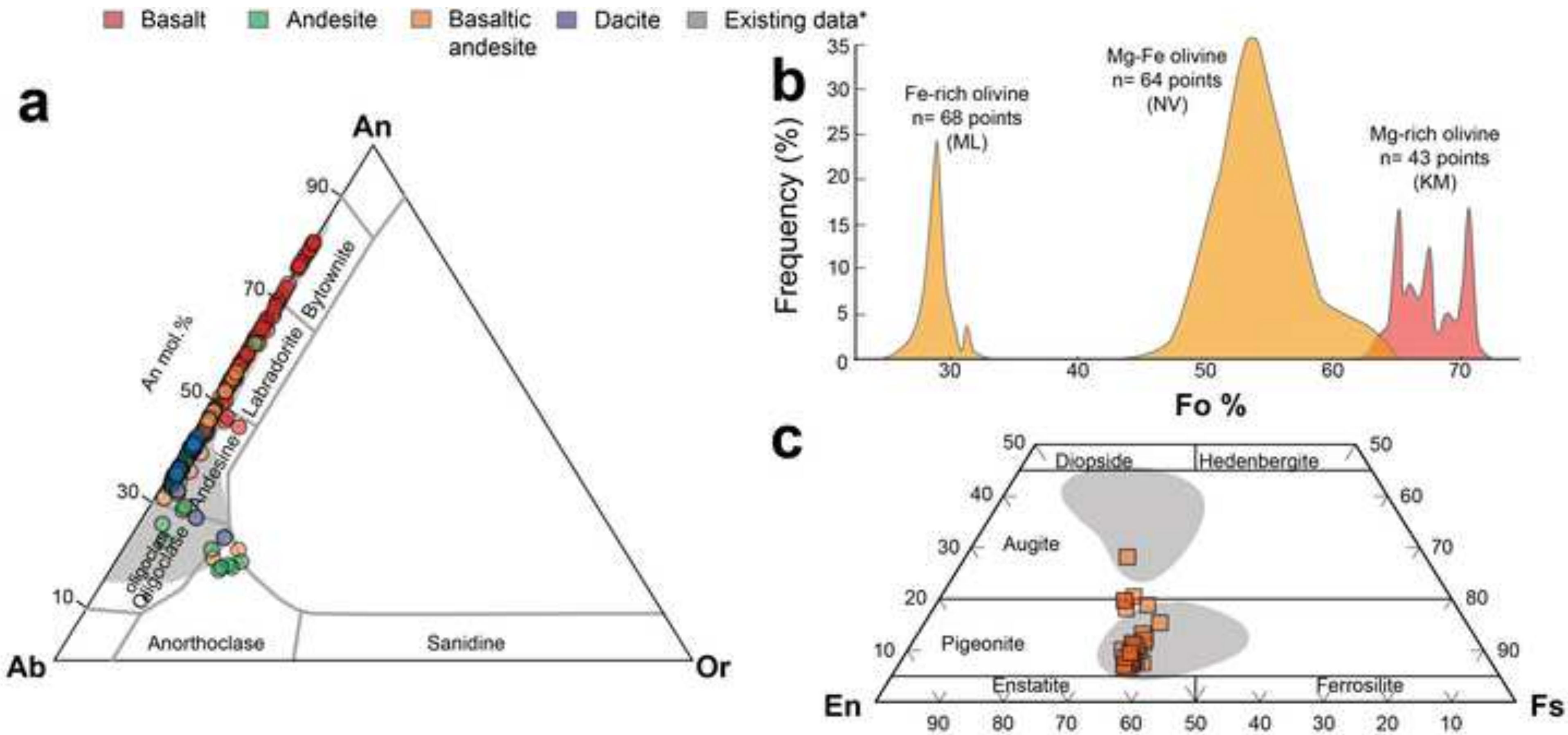

Figure 9

Click here to access/download;Figure;Fig. 9.jpg

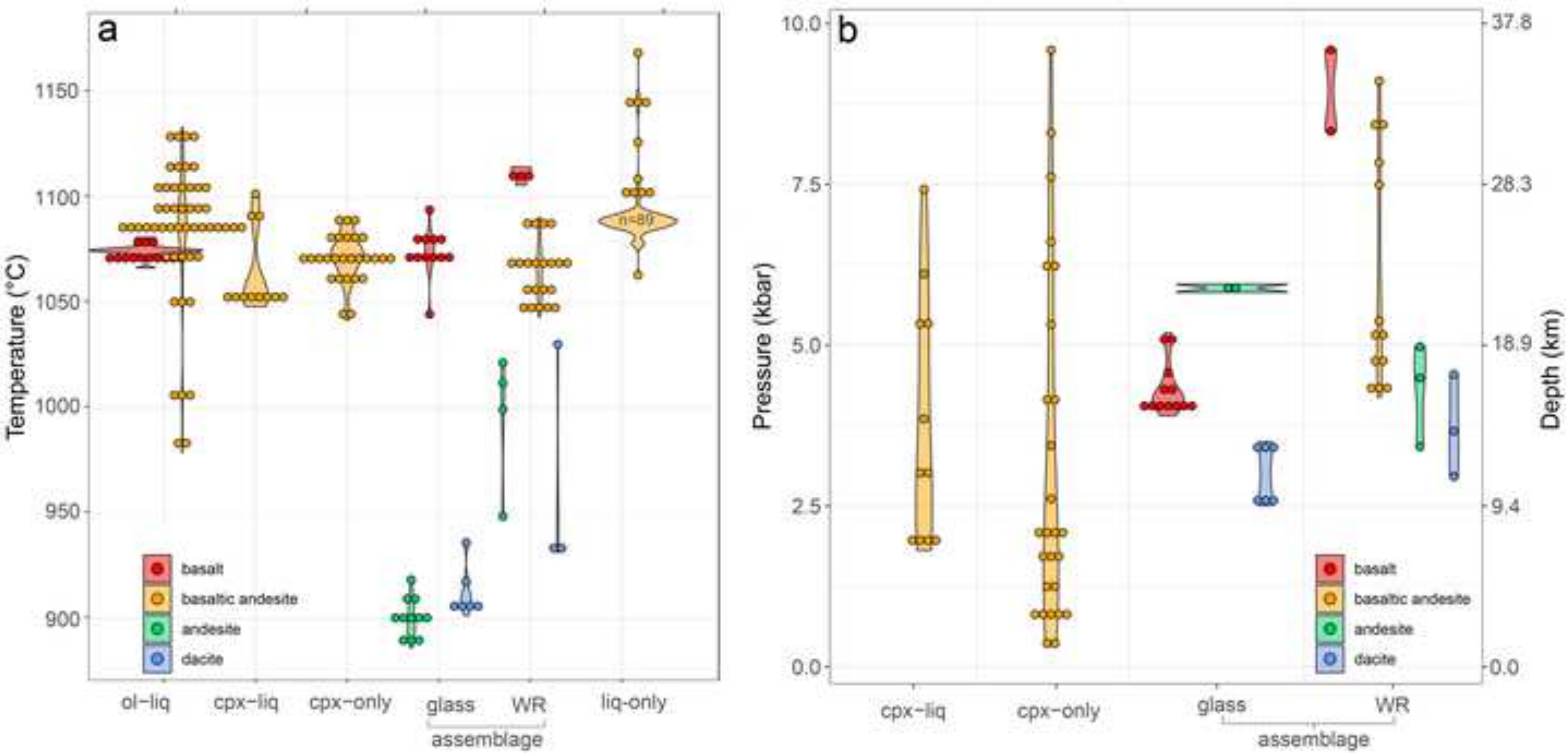

Figure 10

Click here to access/download;Figure;Fig. 10.jpg

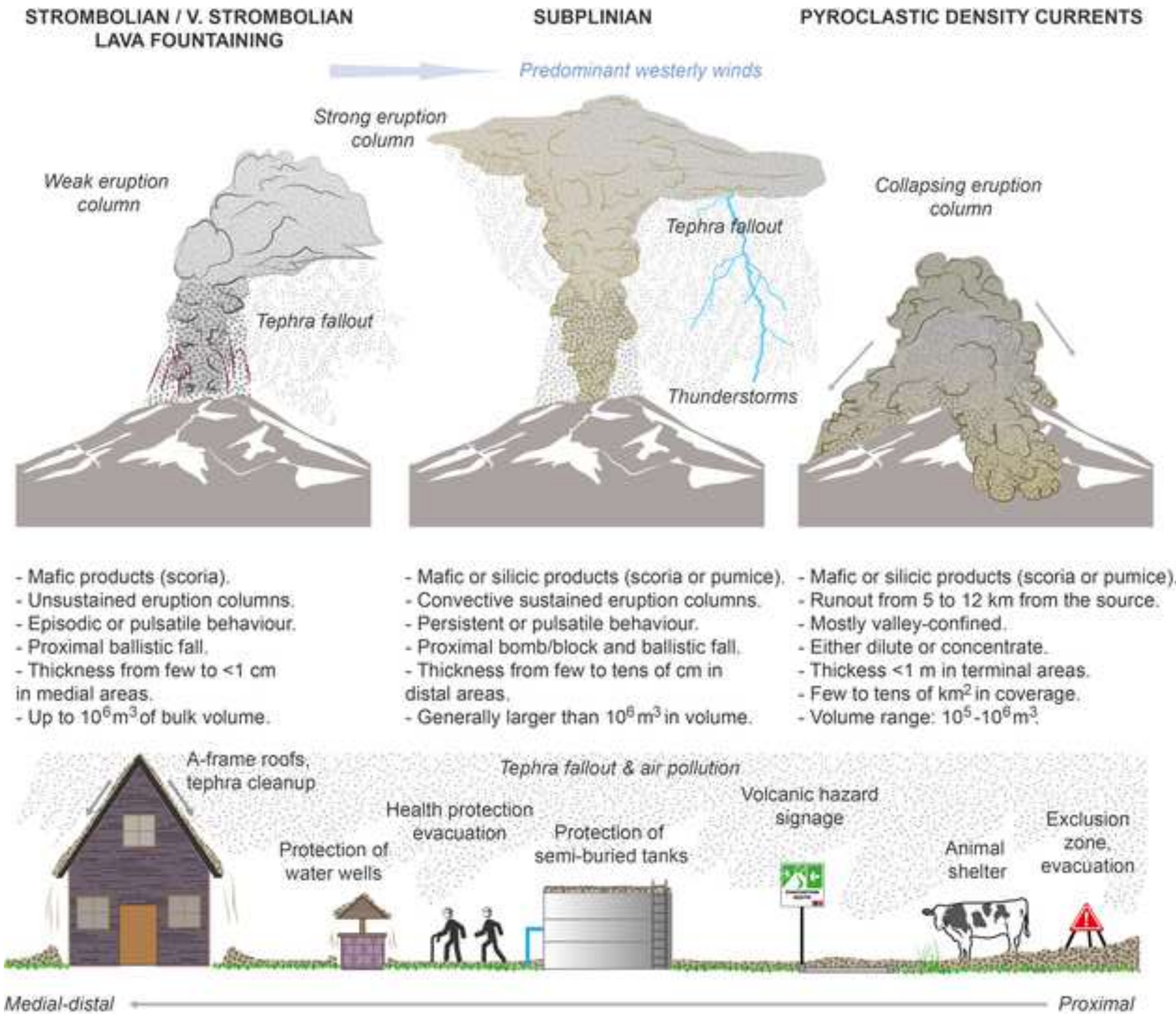

Table 1: Stratigraphic and sedimentologic characteristics of the different tephra units described in this contribution. The corresponding unit ages were correlated from *Polanco (1998) and **Gilbert et al. (2014).

UNIT		AGE	DESCRIPTION	KEY SITES
Navidad	NV	1988-1990 CE	The 1988-90 Navidad Tephra fall deposit (NV) covers most of the present-day landscape towards the east-southeast of the LTVC. A few hundred metres from the Navidad cone, the deposit is >100 cm and it decreases to a few cm–thick at 20 km distance (Naranjo et al. 1991). It is formed by black subrounded to blocky medium-to-fine lapilli scoria and small proportions of oxidised accessory lithics (<5%).	LQ34
Malalcahuello	ML	231-138 BP	The Malalcahuello unit consists of two beds. The lower one is a fine-to-medium lapilli tephra fall deposit ranging from 10 to 15 cm in thickness. It contains c. 20-60% subangular lithics, 30-60% subrounded vesicular scoria and 10-20% subangular to subrounded dense scoria. The upper bed is 20-40 cm thick and consists of a fine-to-medium ash matrix that contains 10-15% scoria lapilli. All the scoria is weathered and presents a yellow to orange color. Charcoal fragments are ubiquitous within the upper bed.	LQ1, LQ19, LQ27, LQ46
Cautín	CU	*194-162 BP	It is usually the present-day erosive surface towards the south-southeast of the LTVC. It greatly varies from individual scattered scoria fragments, likely resulting from surface aeolian deflation of the original tephra bed to a thick sequence of scoria layers, as in LQ36- LQ38 (Fig. 3), that rapidly thins out with distance. The LQ36 sequence is 245 cm–thick and consists of four ungraded coarse lapilli scoria beds containing scattered bombs, while only ~0.7 km southeast, it has decreased to 127 cm–thick and is formed by two instead of four layers and to a single 60 cm–thick deposit at LQ38.	LQ18, LQ29, LQ33, LQ35, LQ36, LQ37, LQ38
Külleg	KL		A 30 cm thick deposit composed of light brown, fine to medium pumice lapilli with normal grading, containing scattered pumice bombs with reddish to orangish exteriors and cm-sized subrounded vesicles.	LQ37
Corralco	CO		At LQ33, CO is a 60 cm–thick scoria deposit consisting of basal intercalation of medium lapilli and cm–thick ash layers (5 cm–thick), with a middle massive unit of ungraded medium coarse lapilli (35 cm–thick). There, the upper 20 cm show intercalations of medium-to-coarse lapilli and ash layers. As in LQ18, more distal outcrops display a single layer with overall normal grading and medium to coarse lapilli. In all the exposures (Fig. 3), CO is brown to black-reddish due to weathering of juvenile scoria.	LQ18, LQ29, LQ33, LQ36, LQ37, LQ38
Wikür	WK		It is a 22-cm thick deposit. The basal 6 cm consists of a black, fine lapilli scoria layer grading to a fine-to-medium lapilli pumice layer of 9 cm thick, with reverse grading and clear brown color. The upper layer is 7 cm thick and contains fine-to-medium brown lapilli pumice.	LQ18
Pumakuñ	PU		It is a bedded which contains seven layers. It has only been described at LQ37 (Fig. 3). It is composed of clear brown scoria lapilli layers and ~15% of angular oxidised lithics, which is coarse to the basal layers and fine to medium lapilli in the upper layers.	LQ18, LQ36, LQ37
Kurütrufken	KT		In LQ18 and LQ33 the latter site, it consists of a 15 cm-thick basal layer of black coarse ash to fine scoria lapilli and another 30 cm of ash matrix-supported lapilli clasts developing cross-bedding structures.	LQ18, LQ33

Alikura (*Va/Vb*)**	AK	**1,294- 391 BP	At LQ33 it forms a 69 cm-thick clear grey to clear yellow lapilli pumice. The very base of the deposit is a single layer of 0.5-0.7 cm, 100% lithic clasts, ~95 % consisting of angular dense porphyritic lava fragments, with ~5% oxidised clasts. It is overlaid by 34 cm of medium to fine lapilli and coarse ash layers organised in rhythmic intercalations. In contrast, the middle 25 cm corresponds to an accumulation of coarse lapilli to bomb-sized pumices with pink interiors. The upper 9 cm are of intercalated coarse ashes and fine pumice lapilli and are generally reworked showing paleochannels and wavy top. At LQ18, it only preserves its medium and top section and starts with pumice bombs up to 18 cm long at the bottom, which lie within an intercalation of 2-4 cm-thick pumiceous lapilli and ash layers give a total of 30 cm-thick. Other thick exposures are also found at LQ36 and LQ37 (56-60 cm, respectively; Fig. 3), whereas distal facies are also observed at LQ29, where the 7 cm deposit consists of fine lapilli to coarse ash pumice particles of white to clear grey colour. Two outcrops studied directly southwards from Lonquimay volcano in Malalcahuello (LQ19 and LQ27) also expose a similar tephra with thicknesses < 10 cm (Fig. 3).	LQ18, LQ19, L127, LQ33, LQ36, LQ37
Kurumawün	KM		It comprises several beds of medium to coarse scoria lapilli, with a general normal grading, occasionally exhibiting bombs in the central part of the deposit. At site LQ36, these bombs are fusiform and may reach up to 45 cm long, whereas at LQ18 they reach 17 cm long. As in LQ29, the massive bottom unit (c. 14 cm-thick) contains up to ~40% dense angular lithics, some of them oxidised, and ~60% black fine scoria lapilli. The middle and top units consist of rhythmic intercalations of fine-to-coarse lapilli and coarse ash beds totalling 57 cm. The juvenile material is black, and depending on local weathering, layers can show different brown tonalities	LQ18, LQ29, LQ33, LQ36, LQ38
Kurütrongen	KG		It is a 105 cm thick clast supported deposit composed of angular to subrounded dense clasts, 0.5-1.5 cm in diameter. It is reversely graded in the first 10 cm, then 85 cm of rhythmic layered intercalation with more rounded, grey fine to medium lapilli clasts.	LQ18, LQ33
Kadü	KA		The deposit is clast supported, with clasts of subrounded to subangular dense clasts, with at least 15% of hydrothermally altered particles. Their size ranges from 0.5 to 2.0 cm in diameter. The total thickness is 95 cm.	LQ18, LQ33
Liqkura (*Sb*)**	LI	**4,415 - 2,648 BP	At LQ18, it forms a medium-to-coarse pumice deposit up to 30 cm-thick with normal grading. Occasionally, a 0.5 cm-thick scoria ash layer can be observed at the bottom. At outcrops closer to the main crater (e.g., LQ36), it forms a reversely graded, 60 cm-thick deposit of coarse pumice lapilli, with juvenile clasts being microvesicular and white to clear brown. It also contains nearly 10 % dense lithics, either grey or oxidised. Correlation among other sites is complex due to the poor preservation of this layer.	LQ18, LQ33, LQ36
Dumiñmapu	DU		It is formed by two superposed black to dark grey scoria fall layers. The one to the bottom is composed of massive coarse lapilli with no grading, whilst the upper one contains medium to fine lapilli	LQ33.
Manto Amarillo	MA	*3,778 – 3,262 BP	It is 20 cm-thick, reversely graded, yellowish, medium-to-coarse lapilli pumice deposit (Fig. 2d). It contains <5% oxidised scoria lithics.	LQ19, LQ27, LQ38, LQ44, LQ41, LQ50, LQ51

Pewenkura	PK	*4,632- 3,778 BP	PK can be observed at the thickest pyroclastic sequences, including LQ25, LQ33, LQ36, and LQ38 (Fig. 3), varying in thicknesses between 25 and 100 cm. At LQ38, the unit's base (up to 80 cm thick) is composed of coarse lapilli to bomb sized pinkish banded pumices, with normal or absent grading. To the top, the deposit grades to a black, coarse, angular lapilli scoria bed (up to 20 cm thick).	LQ25, LQ33, LQ36, LQ38, LQ44, LQ41
La Negra	LN	*5,504-5,446 BP	It consists of an old tephra fall deposit, up to 130 cm-thick, composed of ash-to-lapilli sized basaltic-andesite scoria distributed along the Lolco, Cautín, and Naranjo rivers, east of the LTVC (Polanco 1998). Proximal exposures of LN at LQ36 (Fig. 3) consist of its upper section with a thickness of 130 cm, which mainly corresponds to agglutinated black and oxidised fusiform scoria bombs, overlaid by 6 cm of reworked scoriaceous fine ash. Another more distal exposure at LQ41 (Fig. 3) describes a 29-cm thick sequence consisting of 1) A basal intercalation of fine black scoria lapilli and coarse ash layers totalling 8 cm thick, 2) 7 cm of ungraded fine lapilli, overlaid by 3) 9 cm of medium-to-coarse reversely graded black lapilli, and 4) intercalation of grey, brown, and black fine ash layers totalling 5-cm thick	LQ25, LQ33, LQ36, LQ41, LQ44

Table 2: X-ray fluorescence whole-rock geochemistry of analysed samples. The corresponding unit ages were correlated from *Polanco (1998) and **Gilbert et al. (2014). Only the MA unit description and chemistry is taken from Poblete et al. (2025). That chemistry is the average of sample LON-MP-06BM and its duplicate. In their data, Mn and Fe are reported as FeO_t and MnO, respectively. Analysed particle sizes are MA=Medium ash, CA=Coarse ash, FL= fine lapilli, ML= medium lapilli, CL= coarse lapilli, B=bomb, FG=fine gravel (juvenile fragments in alluvial-laharitic deposits). L.O.I. refers to loss on ignition.

Unit	**La Negra**	**Pewenkura**	**Manto Amarillo**	**Dumiñmapu**	**Liqkura**	**Kadü**	**Kurütrongen**	**Kurümawün**	**Alikura**	**Kurütrufken**	**Pumakuñ**	**Wikür**	**Corralco**	**Külleg**	**Cautín**	**Malalcahuello**	**Navidad**
Label	***LN***	***PK***	**MA*** **	***DU***	***LI***	***KA***	***KG***	***KM***	***AK***	***KT***	***PU***	***WK***	***CO***	**KL**	**CU**	***ML***	***NV***
Age	*5,504-5,446 BP	*4,632-3,778 BP	*3,778 – 3,262 BP		**3,778 - 3,262 BP				**1,294-391 BP					*194-162 BP		231-138 BP	1988-90 CE
Sample	LQ33-2	LQ33-3	LON-MP-06BM	LQ33-4	LQ-18-23-2	LQ-18-23-3	LQ18-A	LQ18-B	LQ18-C	LQ18-D	LQ18-F	LQ18-E	LQ18G2	DCPK	LQ18H	LQ1-CAIDA	BMNV90
Type	Subrounded, black, occasionally oxidised vesicular scoria.	Highly vesicular whitish pumice with pink cores / banding	Angular, lapilli-sized pumice with pale-yellow alteration.	Black vesicular subangular scoria with jagged perimeter	Subrounded to subangular vesicular white to grey pumice	Gray, dense, subangular to subrounded scoria	Subrounded to subangular grey to black dense scoria	Subrounded vesicular black scoria, occasionally reddish	Subangular, white to light yellow vesicular pumice	Black to dark blue glass shards and scoria	Grey, dense, subangular to subrounded juvenile scoria	Black vesicular subangular scoria with jagged perimeter	Black vesicular subangular blocky scoria	Light brown pumice bomb with reddish exterior and cm-sized vesicles.	Light brown subangular scoria, in some cases yellowish as consequence of external weathering	Subrounded vesicular yellow scoria, externally weathered	Fusiform andesite scoria bomb
Size	ML	ML	CL	FL	FL	ML	FG	CL-B	CL-B	MA-CA	FL	FL-ML	ML	B	ML	FL-ML	B
SiO_2	55.14	62.43	61.50	54.71	65.95	60	54.79	49.26	60.62	54.09	58.3	50.48	50.42	62.79	58.02	53.82	55.56
TiO_2	1.23	0.88	0.83	1.38	0.44	1.08	1.17	1.32	0.62	1.47	0.95	1.52	1.52	0.46	0.77	0.94	1.45
Al_2O_3	17.61	13.09	15.92	16.02	14.25	15.44	18.1	17.15	16.6	17.16	17.54	18.25	18.48	16.11	17.25	18.49	17.19
Fe_2O_3	10.44	8.84	8.08	10.64	5.26	8.22	10.06	11.67	7.48	11.55	9.44	12.27	12.82	6.71	9.19	10.2	10.57
Mn_2O_3	0.22	0.26	0.21	0.21	0.17	0.23	0.34	0.36	0.34	0.44	0.38	0.43	0.39	0.31	0.37	0.41	0.37
MgO	2.99	1.23	1.05	2.97	0.84	2.05	2.65	3.67	0.94	2.74	1.54	2.75	3.2	0.49	0.88	1.88	2.6
CaO	7.21	4.46	3.94	7.15	3	5.03	6.1	7.74	3.49	6.17	4.54	6.18	6.77	2.71	3.61	5.3	5.85
Na_2O_3	4.05	4.47	5.10	4.3	5.55	5.54	4.62	3.76	5.31	4.75	5.03	3.85	3.83	5.56	5.07	4.47	5.1
K_2O	0.61	1.29	1.46	0.76	1.33	0.94	0.81	0.5	1.46	0.81	1.14	0.67	0.55	1.61	1.33	1	0.88
P_2O_5	0.18	0.28	0.30	0.2	0.15	0.28	0.27	0.18	0.16	0.32	0.24	0.27	0.25	0.12	0.3	0.25	0.32
SO_3	0.02	0	0	0	0.02	0.02	0	0	0	0	0	0	0.1	0	0.12	0	0.15
Total	99.71	97.23	98.38	98.35	96.97	98.82	98.91	95.61	97.02	99.5	99.1	96.67	98.34	96.87	96.91	96.76	100.04
L.O.I.	0.6	2.1	1.46	0.9	3	0.8	1	1.6	2.1	0.3	1.7	3.2	2.5	1.9	2.9	3.1	0.5

Declaration of interests

☒The authors declare that they have no known competing financial interests or personal relationships that could have appeared to influence the work reported in this paper.

☐The authors declare the following financial interests/personal relationships which may be considered as potential competing interests:

CRediT authorship contribution statement

JER: Writing – original draft, Writing – review & editing, Visualization, Methodology, Investigation, Formal analysis, Data curation, Conceptualization. **FC:** Writing – review & editing, Methodology, Investigation, Formal analysis. **LR:** Investigation, Formal analysis, Data curation. **AG:** Methodology, Investigation, Formal analysis. **EP:** Writing – review & editing, Visualization, Conceptualization. **FVP:** Investigation, Formal analysis, Writing – review & editing, Visualization. **EM:** Methodology, Investigation, Formal analysis. **JAN:** Data curation, Conceptualization. **AF:** Methodology, Investigation, Formal analysis. **GW:** Writing – review & editing, Methodology, Investigation, Formal analysis, Conceptualization. **JB:** Methodology, Investigation, Formal analysis, **AC:** Investigation, Formal analysis, Writing – review & editing. **MP:** Investigation, Formal analysis, Writing – review & editing, **IR:** Writing – review & editing.

Supplementary Material 1

Click here to access/download

Supplementary Material

Supplementary Material 1.xlsx

Click here to access/download
Supplementary Material
Supplementary Material 2.docx

Click here to access/download
Supplementary Material
Supplementary Material 3.xlsx

Click here to access/download
Supplementary Material
Supplementary Material 5.xlsx

Click here to access/download
Supplementary Material
Supplementary Material 6.xlsx

Supplementary Figure 1

Supplementary Figure 2

Click here to access/download
Supplementary Material
Supplementary Fig. 2.jpg

Supplementary Figure 3